Mechanisms underlying contrast-dependent orientation selectivity in mouse V1

Wei P. Dai[a,b], Douglas Zhou[b,c,d,1], David W. McLaughlin[e,f,g,h,i,1], and David Cai[b,c,d,e,f,g,j]

[a]School of Physics and Astronomy, Shanghai Jiao Tong University, Shanghai 200240, China; [b]Institute of Natural Sciences, Shanghai Jiao Tong University, Shanghai 200240, China; [c]School of Mathematical Sciences, Shanghai Jiao Tong University, Shanghai 200240, China; [d]Ministry of Education Key Laboratory of Scientific and Engineering Computing, Shanghai Jiao Tong University, Shanghai 200240, China; [e]Courant Institute of Mathematical Sciences, New York University, New York, NY 10012; [f]Center for Neural Science, New York University, New York, NY 10012; [g]New York University Shanghai, Shanghai 200122, China; [h]NYU Tandon School of Engineering, New York University, Brooklyn, NY 11201; [i]Neuroscience Institute of NYU Langone Health, New York University, New York, NY 10016; and [j]NYUAD Institute, New York University Abu Dhabi, Saadiyat Island, Abu Dhabi, United Arab Emirates

Contributed by David W. McLaughlin, September 13, 2018 (sent for review November 2, 2017; reviewed by David Hansel and Michael P. Stryker)

Recent experiments have shown that mouse primary visual cortex (V1) is very different from that of cat or monkey, including response properties—one of which is that contrast invariance in the orientation selectivity (OS) of the neurons' firing rates is replaced in mouse with contrast-dependent sharpening (broadening) of OS in excitatory (inhibitory) neurons. These differences indicate a different circuit design for mouse V1 than that of cat or monkey. Here we develop a large-scale computational model of an effective input layer of mouse V1. Constrained by experiment data, the model successfully reproduces experimentally observed response properties—for example, distributions of firing rates, orientation tuning widths, and response modulations of simple and complex neurons, including the contrast dependence of orientation tuning curves. Analysis of the model shows that strong feedback inhibition and strong orientation-preferential cortical excitation to the excitatory population are the predominant mechanisms underlying the contrast-sharpening of OS in excitatory neurons, while the contrast-broadening of OS in inhibitory neurons results from a strong but nonpreferential cortical excitation to these inhibitory neurons, with the resulting contrast-broadened inhibition producing a secondary enhancement on the contrast-sharpened OS of excitatory neurons. Finally, based on these mechanisms, we show that adjusting the detailed balances between the predominant mechanisms can lead to contrast invariance—providing insights for future studies on contrast dependence (invariance).

orientation selectivity | contrast invariance | contrast dependence

The front end of the visual system in the cortex, the primary visual cortex (V1), has proven for cat and monkey to be appropriate for large-scale computational modeling—primarily because of the rich collection of experimental measurements on V1 that biologically constrain these models. These large-scale models have then been used to suggest potential mechanisms for various response properties in cat (or monkey) V1, such as orientation selectivity (OS) (1, 2). Individual neurons in V1 respond preferentially to the orientations of edges in the visual scene. This orientation preference is measured by the neuron's orientation tuning curve, a graph of the neuron's firing rate versus the orientation of the visual stimulus. The tuning curve is (usually) uni-modal, with a peak at "preferred orientation" (PO) and troughs at the "orthogonal orientation" (OO). Its half-width at half-maximum, the tuning width, is one measure of the neuron's OS. Although neurons' firing rates often increase with the contrast of the visual stimuli, surprisingly, the OS in cat (or monkey) is found to be approximately contrast-invariant (3, 4). Many theoretical (5–8) and experimental (9–11) works have addressed the source of this contrast invariance. In mouse, despite its poor visual acuity, neurons in V1 are surprisingly well-tuned for orientation (12–14), with tuning widths similar to those of cat or monkey. A series of experiments (13, 15, 16), as well as a behavioral vs. neuronal discrimination experiment (14), have shown that instead of contrast-invariant OS, excitatory (inhibitory) neurons in mouse V1 exhibit contrast-sharpened (broadened) OS.

Sophisticated optogenetic tools for mouse are providing even more comprehensive experimental data than are available for cat or monkey. Visual neuroscientists now have a detailed circuit structure of mouse V1 (17–21) and rich measurements of its response properties (12, 13, 22, 23). Thus, it is time for theorists to develop comprehensive large-scale models of mouse V1, which may unravel the mechanism underlying its response properties, such as the contrast-dependent OS.

There are significant hardwired differences between mouse V1 and cat (or monkey) V1, which we incorporate into our model. Neurons of mouse V1 receive only weakly tuned input (19) from the lateral geniculate nucleus (LGN); the receptive fields (RF) of this input have strongly overlapping ON and OFF subregions (15, 23), and the diameters of the LGN RFs are very large—averaging more than 10° for excitatory neurons and 20° for inhibitory neurons (23) (Fig. 1 *A*, *Top Left*), while in cat and

Significance

Recently, sophisticated optogenetic tools for mouse have enabled many detailed studies of the neuronal circuits of its primary visual cortex (V1), providing much more specific information than is available for cat or monkey. Among various other differences, they show a striking contrast dependency in orientation selectivity in mouse V1 rather than the well-known contrast invariance for cat and monkey. Constrained by the existing experiment data, we develop a comprehensive large-scale model of an effective input layer of mouse V1 that successfully reproduces the contrast-dependent phenomena and many other response properties. The model helps to probe different mechanisms based on excitation–inhibition balance that underlie both contrast dependencies and invariance, and it provides implications for future studies on these circuits.

Author contributions: W.P.D., D.Z., D.W.M., and D.C. designed research; W.P.D. performed the research; W.P.D., D.Z., D.W.M., and D.C. contributed new reagents/analytic tools; W.P.D., D.Z., D.W.M., and D.C. analyzed data; and W.P.D., D.Z., D.W.M., and D.C. wrote the paper.

Reviewers: D.H., Centre de Neurophysique, Université Paris Descartes; M.P.S., University of California San Francisco Medical Center.

The authors declare no conflict of interest.

Data deposition: The source code for our model have been deposited on GitHub (https://github.com/g13/mouseV1).

[1]To whom correspondence may be addressed. Email: david.mclaughlin@nyu.edu or zdz@sjtu.edu.cn.

This article contains supporting information online at www.pnas.org/lookup/suppl/doi:10.1073/pnas.1719044115/-/DCSupplemental.

Published online October 18, 2018.

NEUROSCIENCE

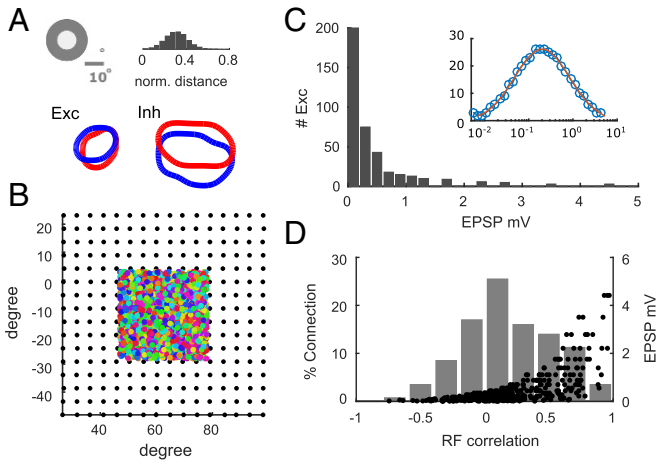

Fig. 1. Simulation setup. (*A*, *Top Left*) Typical size of an LGN RF in mouse vs. that of a monkey, a small point to the right. (*Top Right*) Gaussian distribution of normalized distance between subregions with a mean of 0.305 and SD of 0.1. (*Bottom*) Examples of inherited RF from LGN for V1 excitatory (Exc) and inhibtory (Inh) neurons with the ON subregion (red) and OFF subregion (blue). (*B*) A patch of V1 neuron (colored dots) plotted on a grid of LGN cells (black dots) in a visual field. Different colors indicate different POs. (*C*) Histogram of EPSPs to excitatory neurons with log-normal distribution. *Inset* shows the same data but with log *x* axis, with a mean of 0.45 mV and SD of 0.68 mV. (*D*) The distribution of EPSPs (dots) received by an example excitatory neuron over the pairwise RF CC distribution of its presynaptic excitatory neurons (background).

monkey the subregions are more segregated (24, 25), with diameters mostly below 1°. Cat and monkey V1 have ordered maps of PO, tiled by orientation pinwheels (26); in contrast, mouse V1 has a disordered "salt and pepper" map of PO (27). Layer 2/3 (L2/3) in cat and monkey V1 is dominated by "complex" (nonlinear) neurons (28, 29). However, in mouse, "simple" (linear) neurons make up the majority ($70 \sim 80\%$) of excitatory neurons in L2/3 and L4, and most of the inhibitory neurons are complex (12). An early lesion experiment on mouse has shown that LGN axons arborize in L2/3 as well as in L4 (30). The layer-specific data from ref. 12 also indicate that the linearity ($F1/F0$) distribution, the OS distribution, and the RF size are similar in L2/3 and L4. Taken together, the common properties shared by L2/3 and L4 in mouse provide certain justification for combining L2/3 and L4 into a single "effective layer." It is also found that the excitatory neurons selectively receive strong excitatory postsynaptic potentials (EPSPs), ~ 4.5 mV, from neurons with similar RFs (21), while an amplitude of $1 \sim 2$ mV is considered large in cat V1 (31). The inhibitory population in mouse V1 receives strong input from the LGN as shown in refs. 32 and 33, while such data are rather scarce for cat and monkey. Inhibitory neurons in mouse V1 receive strong input from cortical excitatory neurons regardless of their PO (17), and they show much poorer OS (22, 34) than the inhibitory neurons in cat or monkey V1 [but see a sharply tuned subtype (35)]. These hardwired differences suggest that different mechanisms may underlie the response properties of mouse V1 from those of cat or monkey.

Here we construct a comprehensive large-scale, biologically constrained by experimental data, model of an effective input layer of mouse V1 from which many experimentally observed response properties emerge; then we analyze in detail the contrast-sharpening (contrast-broadening) of the OS of excitatory (inhibitory) neurons and extract the underlying mechanisms from the model by probing the excitation–inhibition (E–I) balances; based on the extracted mechanisms, we further identify the adjustments to the E–I balance and the selectivity of connectivity that result in contrast invariance. Thus, with the experimentally constrained nature of the model, our result bears insights for future studies on contrast invariance and contrast dependence.

Methods

Our model consists of a grid of 16×16 LGN cells covering a visual field of $75^\circ \times 75^\circ$ and a patch of 10,800 V1 neurons in a single layer compressed from L2/3 and L4, with an effective neuronal density of $2.9 \times 10^4/\text{mm}^2$ (36). The V1 patch is a uniform mixture of a 120×72 grid of excitatory neurons and a 60×36 grid of inhibitory neurons, such that the E-I ratio is kept at 4 : 1. The model is described with sufficient details in *SI Appendix* to enable the reproduction of simulation results; the source code can be found at https://github.com/g13/mouseV1. Here we only present an overview of the model setup, emphasizing its salient features including each that distinguishes mouse V1 from that of cat or monkey, as summarized in the Introduction.

LGN Layer, Mapping to V1. The LGN input to V1 is modeled with a linear–nonlinear Poisson paradigm. Drifting sinusoidal waves with a temporal frequency of 4 Hz, a spatial frequency of 0.04 cycle per degree, and contrasts of 12.5%, 25%, 50%, and 100% are used as the external inputs to LGN. We adopt the parameters and a typical gain curve from the experiment on mouse dorsal LGN cells (37) to construct a spatiotemporal separable center-surround RF kernel and a static nonlinearity, respectively. We apply the nonlinearity on the result of the convolution of the RF kernel with the input. Its output is then used as the rate of a Poisson process from which we form the spike train inputs to V1 neurons.

Each V1 neuron is connected postsynaptically to a collection of LGN cells with two largely overlapping subregions, one of ON LGN cells and the other of OFF LGN cells. Taken together, these two subregions form the RF of the V1 neuron inherited from LGN. The extent of overlap is described by a normalized distance between the two subregions' tentative centers (see *SI Appendix*). The normalized distance has a Gaussian distribution across the population (Fig. 1 *A*, *Top Right*), whose mean and SD are derived from the experiments in refs. 19, 23. Examples of V1 neurons' RFs resulting from such connections are shown in Fig. 1 *A*, *Lower*. Notice the size difference between excitatory and inhibitory RFs, as multiple experiments have shown for mouse V1 that inhibitory neurons receive about twice the LGN input received by excitatory neurons (32, 33). To implement this experimental result, we assume the following: (*i*) an increase in LGN input to inhibitory neurons through an increase in the number of presynaptic LGN cells projecting to the inhibitory neuron (~ 30 to each inhibitory neuron, ~ 15 to each excitatory neuron), and (*ii*) the increase in LGN cells extends along the major axes of the ON and OFF subregions. We make these two detailed assumptions in the model to show a more prominent contrast-broadening effect in inhibitory neurons; however, they are not essential (see *SI Appendix*, Fig. S2).

Cortical Layer. The salt and pepper distribution of POs in mouse V1 (Fig. 1*B*) is modeled by presetting each V1 neuron's RF with a uniform distribution of POs. The probability of intracortical connections decays over distance through an isotropic Gaussian distribution for both excitatory and inhibitory neurons. Periodic boundary conditions are applied when the connection distance exceeds the boundary of the V1 patch, and all of the neurons are used in analysis. The total connection probability to an excitatory neuron is sparse—15% (20) (~ 400 *E* and ~ 100 *I* neurons). Excitatory neurons in L2/3 of mouse V1 are known to have larger probabilities to connect with excitatory neurons that share similar RFs and POs (20, 21), and a similar preferential connectivity between excitatory neurons ($E \to E$) is likely to exist in L4 as well (19). Likewise, the same connection preference has also been implied for the $I \to E$ connections by Tan et al. (38). Thus, we introduce another Gaussian distribution to capture these orientation preferential couplings to excitatory neurons (details available in *SI Appendix*). In addition to the orientation preferential connection probability, Cossell et al. (21) found the $E \to E$ connection strengths to be dependent on the pairwise correlation coefficient (CC; see *SI Appendix* for its definition) of RFs, and the EPSPs have a highly skewed distribution toward a larger amplitude (21). In this model, we implement this dependency with a log-normal distribution (Fig. 1*C*, comparable with the experiment in ref. 21; the *Inset* figure shows the same data in log-scale). One example of an excitatory neuron's presynaptic EPSP distribution for such a setup is shown in Fig. 1*D*, where the background histogram gives the distribution of RF CC with its presynaptic neurons (higher value indicates a more similar RF). Note that, although few in number, those with larger RF CC produce much larger EPSP amplitudes such that, on average, 50% of the cortical excitation is contributed by those 18% of presynaptic neurons with larger RF CC, comparable with the experiment in ref. 21.

On the other hand, the $E \rightarrow I$ connections are found experimentally to be much stronger, more numerous, and with no selectivity over orientation, as shown by Bock et al. (17). Consistently, in our model, the corresponding connection probability is set at 60% ($\sim$1000 E and $\sim$300 I neurons) and only depends on distance, with connection strength on par with the largest excitatory-to-excitatory connection strength.

Each V1 neuron is represented as a conductance-based exponential integrate-and-fire point neuron model (39) with frequency adaptation. The adaptation is modeled by a self-inhibitory conductance g_{adap} that only increases when the neuron itself fires. The voltage dynamics of the ith neuron in the kth population is thus governed by

$$\begin{aligned}\frac{dV_k^i}{dt} &= -g_{L,k}\left(V_k^i - V_L\right) + g_{L,k}\Delta_T \exp\left(\frac{V_k^i - V_T}{\Delta_T}\right)\\ &\quad + I_{syn,k}^i(t) - g_{adap}^i(t)\left(V_k^i - V_I\right),\\ I_{syn,k}^i(t) &= -\left(g_{E\rightarrow k}^i(t) + g_{LGN\rightarrow k}^i(t)\right)\left(V_k^i - V_E\right)\\ &\quad - g_{I\rightarrow k}^i(t)\left(V_k^i - V_I\right), \qquad [1]\end{aligned}$$

where $k = E$ or I. $g_{L,E} = 50\ \mathrm{s}^{-1}$ and $g_{L,I} = 70\ \mathrm{s}^{-1}$ are the leak conductance of excitatory and inhibitory neurons, respectively. $V_L = 0$, $V_E = 2.8$, and $V_I = -0.4$ are the dimensionless reversal potentials. $\Delta_T = 0.4375$ concerns the voltage slope of spike initiation, and $V_T = 1$ is the soft threshold; the hard threshold where V_k^i is reset to V_L is set to 4.375. $I_{syn,k}^i$ is the total synaptic current, where the excitatory ($g_{E\rightarrow k}^i$), LGN ($g_{LGN\rightarrow k}^i$), and inhibitory ($g_{I\rightarrow k}^i$) conductances are summed over all spikes of the corresponding presynaptic neurons. The temporal profiles of all of the conductances are modeled by alpha functions (see *SI Appendix*). A modified Runge–Kutta scheme in ref. 40 is used in the simulation.

We use $1 - \mathrm{CV} = \left|\Sigma_j r_j e^{2i\theta_j}\right| / \Sigma_j r_j$, where CV is circular variance and r_j is the firing rate with input orientation θ_j, to describe the overall sharpness of a tuning curve (12, 13); a larger $1 - \mathrm{CV}$ indicates a sharper OS.

Results

Our effective input-layer model largely reproduces the response properties of the V1 network, including the distributions of firing rates, tuning widths, response modulation F1/F0 (simple and complex neurons), and interspike intervals. These are presented, discussed, and compared with experimental observations in *SI Appendix*. In the main text, we focus on the results of contrast-related OS properties.

Contrast Dependency. The contrast-sharpening (contrast-broadening) of OS in excitatory (inhibitory) neurons is captured by the model, as shown in Fig. 2. Fig. 2 *A* and *B* show two sets of tuning curves with various firing rate levels, for excitatory and inhibitory neurons, respectively. Both contrast-sharpening and contrast-broadening phenomena are present saliently in Fig. 2 *C* and *D*, where population-averaged tuning curves at different contrasts are normalized and aligned to the optimal input orientation for excitatory and inhibitory populations, respectively. The phenomena of contrast dependencies are also apparent in terms of $1 - \mathrm{CV}$ in Fig. 2 *E* and *F*, as the $1 - \mathrm{CV}$ distribution of excitatory and inhibitory populations are separated by the dotted contrast-invariant line.

The tuning curves of the conductances impinging on excitatory and inhibitory neurons are shown in Fig. 2 *G* and *H*, respectively, where all tuning curves are normalized to their own maxima, except the first temporal harmonic of the LGN conductance, $F1$ (magenta), which is normalized by its mean value, $F0$. The $F1$ part of the LGN conductance shows negligible signs of contrast dependency and is only weakly tuned for orientation. However, as shown in Fig. 2*G*, the tuning curves of cortical excitatory conductance (red, $g_{E\rightarrow E}$) are clearly contrast-sharpened, while the inhibitory conductance (blue, $g_{I\rightarrow E}$) is contrast-broadened, comparable with the experiment in ref. 13. Other input conductances, such as $g_{E\rightarrow I}$, are orientation-unspecific (Fig. 2*H*), which is consistent with the experiment in ref. 17 (see *SI Appendix*, Fig. S6). The magnitude of the excitatory conductance $g_{E\rightarrow I}$ (Fig. 2*I*) increases substantially with contrast, surpassing and then overwhelming the LGN conductance. This strong and orientation-unspecific cortical excitation to the inhibitory population is crucial in the model for the contrast-broadening of OS in inhibitory neurons, which then give rises to the broadening of $g_{E\rightarrow I}$ with increasing contrast.

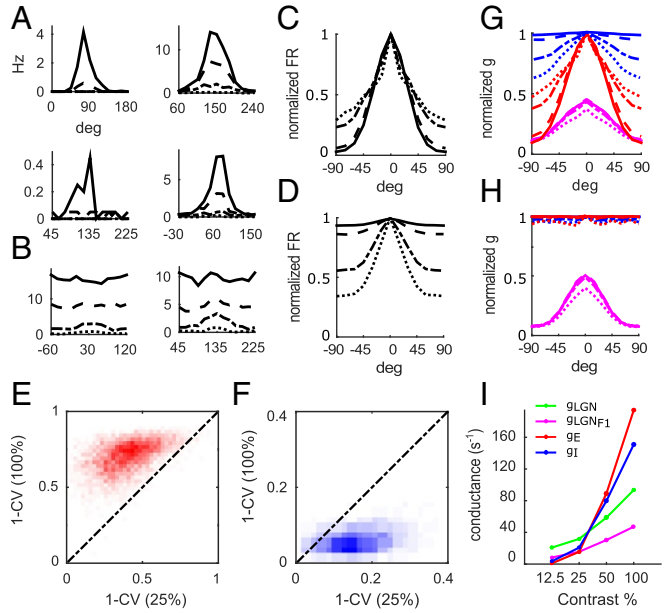

Fig. 2. Simulation results. Tuning curves of 12.5%, 25%, 50%, and 100% contrasts are in dotted, dot-dashed, dashed, and solid lines, respectively. (*A* and *B*) Examples of firing rate tuning curves of excitatory and inhibitory neurons, respectively. (*C* and *D*) Population averages of excitatory and inhibitory neurons' firing rate tuning curves, respectively. Every tuning curve is normalized by its maximum firing rate. (*E* and *F*) Heatmaps for the density distribution of $1 - \mathrm{CV}$ with contrast at 25% vs. 100% for the firing rate tuning curves of excitatory and inhibitory populations, respectively. The dot-dashed line indicates contrast-invariant OS. (*G* and *H*) Population averaged, normalized tuning curves of conductances in excitatory and inhibitory neurons, respectively. The legend follows *I*. The total LGN conductance is not shown here, since it is flat and overlapped at $y = 1$. Instead, we plot the F1 component of the LGN conductance (magenta) normalized to the F0 component. (*I*) Absolute levels of different conductances in the inhibitory population across contrasts corresponding to *H*, with averaged total LGN conductance in green.

Underlying Mechanisms. Next, we describe and analyze the mechanisms underlying the contrast dependencies in our model, as illustrated in Fig. 3*A*, where input orientations are indicated by different colors. At low contrasts, since the excitatory firing rates are low, feed-forward input (from LGN) makes up the majority of the excitation (Fig. 2*I*). Thus, the tuning curves are largely shaped by the LGN inputs, which themselves are only weakly tuned due to the strong overlap between the ON and OFF subregions. In addition, the orientation-specific $I \rightarrow E$ inhibitory connections result in weakly tuned $g_{I\rightarrow E}$ that helps to lift the cap on the excitatory firing rates at OO, while limiting the firing rate at the PO. Thus, at low contrasts, the excitatory neurons' tuning curves are relatively broad.

At higher contrasts, increased cortical firing rates cause the cortical drive to become stronger. Therefore, excitatory neurons experience enhanced cortical excitation at PO but only small increases at OO—since excitatory neurons of similar RF and PO are more likely to be connected and connected with stronger EPSPs. This orientation-specific cortical excitation raises the excitatory neurons' responses, especially at PO. Meanwhile,

NEUROSCIENCE

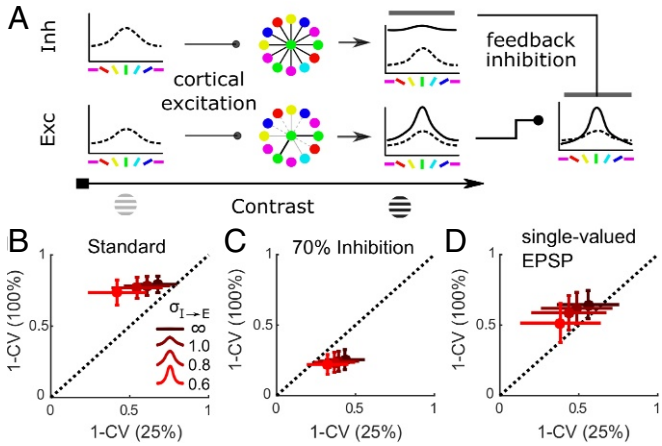

Fig. 3. Underlying mechanisms. (*A*) Diagram of the mechanism for the contrast-dependent phenomena, with excitatory sharpening on *Lower* and inhibitory broadening on *Upper*. The arrow along the *x* axis marks the direction of increasing contrast. Tuning curves at low contrast are indicated by the dotted lines, while the tuning curves at high contrast are in solid lines, and the input orientations are indicated by bars of different colors. Schematic illustrations of excitatory presynaptic connections are shown in between the tuning curves of low and high contrasts. The colored filled circle at each center is an excitatory (inhibitory) neuron of interest, and its presynaptic neurons of different POs (indicated by different colors) are connected with a different strength in dashed gray, solid gray, thin solid black, and thick solid black lines (from weak to strong). (*B*) $1-\mathrm{CV}$ value of the firing rate tuning curves for excitatory populations under 100% contrast vs. 25% contrast, with the same standard parameters used as in Fig. 2, except the SD of $I\to E$ connections, $\sigma_{I\to E}=0.6, 0.8, 1.0, \infty$, as shown in the legend (0.6 is used for Fig. 2). SDs along both axes are shown by the error bars. (*C*) Same as *B*, but with 70% cortical inhibition in excitatory neurons. Connection strengths are adjusted correspondingly. (*D*) Same as *B* but with single-valued EPSP instead of log-normal distributed EPSP.

inhibitory neurons receive much stronger cortical excitation at all orientations, which dominates the LGN input (Fig. 2*I*) and produces high inhibitory firing rates that inflict strong feedback inhibition onto excitatory neurons. This orientation-unspecific cortical excitation results in the broadened OS of inhibitory neurons, which in turn broadens the tuning curves of $g_{I\to E}$. In the meantime, this broadened feedback inhibition pulls down the excitatory neurons' responses at all orientations (more so at OO than that of low contrast). Thus, the OS of excitatory neurons is significantly sharpened.

Both the level of the inhibition ($g_{I\to E}$) and its contrast-broadened profile contribute to the contrast-sharpening of OS in excitatory neurons. To show which property of $g_{I\to E}$ contributes more, we vary the SD of the connection probability of the $I\to E$ connections, $\sigma_{I\to E}$, from 0.6 to ∞ with other parameters unchanged. $\sigma_{I\to E}$ sets the sharpness of the tuning curves of $g_{I\to E}$ at low contrast (illustrated by the legend in Fig. 3*B*), when the inhibitory firing rate is relatively selective (Fig. 2*D*). Since at higher contrast, $g_{I\to E}$ is always flat following the contrast-broadened inhibitory firing rate, the effect of the contrast-broadening of $g_{I\to E}$ is largely determined by $\sigma_{I\to E}$ at low contrast—the smaller $\sigma_{I\to E}$, the larger the effect of the contrast-broadening of $g_{I\to E}$. Thus, the case with $\sigma_{I\to E}=\infty$ represents the complete absence of contrast-broadening in $g_{I\to E}$, since it is flat across all contrasts. The simulation results in Fig. 3*B* show that all of these cases reside above the contrast-invariant line, indicating that the contrast-sharpening phenomenon exists with or without the contrast-broadening of $g_{I\to E}$. On the other hand, if we reduce the overall level of inhibition to 70% by decreasing connection strengths, while keeping the firing level relatively unchanged, none of the cases retains contrast-sharpening (Fig. 3*C*). This indicates that the level of inhibition is more relevant than the contrast-broadening of $g_{I\to E}$. However, the broadened profile of $g_{I\to E}$ does make a (secondary) contribution to the contrast-sharpening of OS in excitatory neurons, for if we quantify the contrast-sharpening effect by the distance to the contrast-invariant line, then stronger contrast-broadening of $g_{I\to E}$ does shift the OS of excitatory neurons toward the stronger contrast-sharpening effect (Fig. 3*B*). Nonetheless, this sharpening effect is not sufficient to overcome the broadening caused by a 30% decrease in the magnitude of inhibition. These results demonstrate that the level of inhibition plays a more important role than the contrast-broadening of $g_{I\to E}$ as mechanisms that underlie the contrast-sharpening of OS in excitatory neurons.

To assess the contribution of the log-normal EPSP distribution to the contrast-sharpening of OS, we set all $E\to E$ connections to have the same strength value as the mean in the original log-normal distribution. As shown in Fig. 3*D*, without the log-normal EPSP distribution, only a very weak contrast-sharpening effect exists, as the values are fairly close to the contrast-invariant line, with the error bars crossing it. Thus, the heterogeneity from the log-normal EPSP distribution is also important for the contrast-sharpening of OS in excitatory neurons, as they compensate an otherwise lower and less tuned cortical excitation. Notice that the populations with smaller $\sigma_{I\to E}$ (stronger contrast-broadening of $g_{I\to E}$) maintain their close distance to the contrast-invariant line, showing that the contrast-broadening of $g_{I\to E}$ has a much less effective role in the contrast-sharpening of OS in excitatory neurons than the standard case shown in Fig. 3*B*. Its actual cause can be attributed to both the weakened preferential excitation due to the single-valued EPSP and a major decrease in the otherwise strong feedback inhibition that is driven by the now less active excitatory neurons (see *SI Appendix* for details).

To summarize, the preferential $E\to E$ connections and their stronger connection strengths, together with strong feedback inhibition, are the primary mechanisms by which the model achieves contrast-sharpening of OS in the excitatory population, while the nonpreferential $E\to I$ connections lead to contrast-broadening of OS in inhibitory neurons.

Discussion

In this work, we construct a large-scale effective input-layer model for mouse V1 under the constraints from experimental data. The model successfully reproduces response properties

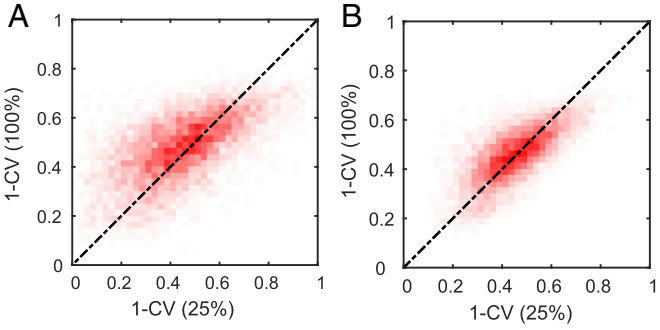

Fig. 4. Contrast-invariant excitatory OS. $1-CV$ value under 100% contrast vs. under 25% contrast for the excitatory firing rates. The dotted lines indicate contrast-invariant OS. (*A*) The log-normal EPSP distribution is replaced with a single-valued EPSP, the same as in Fig. 3*D*; $\sigma_{E\to E}=0.65$ (0.5 in standard case) and $\sigma_{I\to E}=1.0$ are used, and the connection strengths are not changed. (*B*) Eighty percent inhibition also achieves contrast-invariant OS without changes in the connection profile but only with changes in connection strengths ($\sigma_{I\to E}=1.0$).

experimentally observed for mouse V1, including contrast-sharpening (contrast-broadening) of OS in excitatory (inhibitory) populations. We show that strong, highly preferential ($E \to E$) excitation, strong feedback ($I \to E$) inhibition, and strong orientation-unspecific cortical ($E \to I$) excitation are the primary mechanisms underlying the contrast-dependent phenomena in the model and that the effects of the contrast-broadening of $g_{I \to E}$ are secondary for the contrast-sharpening of OS in excitatory neurons.

Previously, theoretical modeling works on mouse V1 of Hansel and Van Vreeswijk (41) and Sadeh and Rotter (42) have throughly discussed the mechanisms of emergent OS from a randomly connected network without an orientation map. These studies focused on contrast invariance and revealed how a small input bias in orientation can be amplified in a balanced network or an inhibition-dominated network, respectively. Another study by Roy et al. (43) explores the parameter space to reproduce experimentally observed OS distributions in mouse V1 at a fixed contrast, and they find it necessary to have orientation preferential $E \to E$ connections. In contrast, we constrain our model by experimental observations of mouse V1 on various input properties (17, 19, 23, 32, 33)—for example, a highly skewed distribution of $E \to E$ connection strengths (21), which depend on pairwise correlation of RFs—and investigate contrast-dependent OS (13) and its possible underlying mechanisms. A simulation-assisted analysis, as discussed in *SI Appendix*, provides additional intuition about the mechanisms underlying the model's performance.

There is an informative analogy between our mouse V1 model and models of monkey V1 (1, 44) where neurons closer to pinwheel centers are more sharply tuned than neurons farther from the centers—because neurons near the centers receive inhibition from the nearby inhibitory neurons with all POs, while those far from the center are inhibited by nearby neurons with similar POs. This process of the distance-dependent "center-broadening" of inhibition (mediated by the inhibitory conductances) resulting in the "center-sharpening" of OS is very similar to the process of the contrast-broadening of $g_{I \to E}$ helping to enhance the contrast-sharpening of OS in excitatory neurons in our mouse model. Consistently, when inhibition is less dominant in the monkey V1 models, center-sharpening of OS is also lessened (44), just as shown by our analysis on the effects of contrast-broadening of $g_{I \to E}$.

Limitations. First, the gain curves of the excitatory neurons are relatively too low at low contrast compared with experimental observations. Second, our model's $1 - CV$ distribution for excitatory neurons represents only a sharply tuned subset of the neurons in the experiments (12, 13) rather than the entire distribution; moreover, in our model, the OS of the excitatory population is substantially sharper than the experimental measurements (19, 45). In an effort to address these two limitations, we have incorporated synaptic depression into the LGN input of the model. We show in *SI Appendix* that this modified model has very similar contrast-dependent phenomena and the same major underlying mechanisms as in our original model but with more realistic gain curves and OS. However, in this modified model, the contrast-broadening of $g_{I \to E}$ conductance is significantly reduced.

Contrast Invariance, With or Without Ordered Maps of PO. The pinwheel-like ordered map of PO in cat (or monkey) V1 versus the random salt and pepper map of PO in mouse V1 is one of the most striking differences between the two anatomically. However, topographically, they have similar selective connectivities based on PO. In monkey, the ordered map of PO implicitly creates selective connectivity since nearby neurons are more likely to be connected than distant neurons and nearby neurons naturally have similar POs in the map. In mouse, an explicit selective $E \to E$ connectivity based on similar POs replaces the implicit selectivity for monkey.

It seems that the explicit connectivity in mouse V1, contributing substantially in producing contrast-sharpening, may be stronger than the implicit connectivity in an ordered map of PO, even though the neuronal density of macaque V1 is about 2.5 times that of a rodent (46), which together with the pooling of neurons (with similar POs) in the ordered map of PO provides a larger reservoir of potential preferential connections than is available to excitatory neurons in mouse V1, which have to search through the uniformly distributed PO. Thus, it is very likely that the much stronger bias in the $E \to E$ connection strengths (21) in mouse V1 overcompensates for the low availability of preferential connections to help achieve contrast-sharpening of OS in excitatory neurons.

Thus, one may wonder whether contrast invariance can be observed if one were to correct the overcompensation of $E \to E$ orientation preference. Indeed, if we moderately weaken the preference of $E \to E$ connections by increasing $\sigma_{E \to E}$ from 0.5 to 0.65 and reduce the strength of their EPSPs (through a single-valued EPSP distribution), contrast invariance in the excitatory population is obtained, as shown in Fig. 4*A*. A major consequence of this relative decrease in excitation is a resulting decrease in feedback inhibition to the excitatory neurons, which decreases sharpening. Therefore, an alternative way to achieve contrast-invariant OS in the model (without explicitly modifying the preferential excitatory connections) is to directly decrease the overall level of inhibition as hinted by Fig. 3*C*. To do this, we follow the scheme used for Fig. 3*C*, keeping the $I \to I$ connection strength constant and decreasing the other connection strengths. Note that we only decrease them moderately so that the overall inhibition is weakened only by $\sim 20\%$, in contrast to the 30% used for Fig. 3*C*. Again, contrast-invariant OS of excitatory neurons is obtained, as shown in Fig. 4*B*.

With these two examples, we demonstrate two ways to produce contrast-invariant OS in the excitatory neurons. Importantly, both methods adjust the E-I balance, by decreasing either the preferential cortical excitation or the feedback inhibition—the two primary and interrelated mechanisms that underlie the contrast-sharpening of OS in excitatory neurons. Thus, with reasonable variability of E-I balances, it is possible that both contrast-invariant and contrast-sharpening of excitatory neurons are actually present in mouse V1, which suggests further experimental studies on contrast dependence of OS in mouse and bears an implication for the understanding of contrast invariance of other species in general.

ACKNOWLEDGMENTS. We thank Louis Tao for initial discussions of this work, and the two referees for their helpful reviews. This research was carried out on the High Performance Computing resources at New York University Abu Dhabi. This work was supported by National Science Foundation in China Grants 11671259, 11722107, 91630208, and 31571071 (to D.Z. and D.C.) and by NYU Abu Dhabi Institute Grant G1301 (to W.P.D., D.Z., and D.C.).

1. McLaughlin D, Shapley R, Shelley M, Wielaard DJ (2000) A neuronal network model of macaque primary visual cortex (V1): Orientation selectivity and dynamics in the input layer 4Cα. *Proc Natl Acad Sci USA* 97:8087–8092.
2. Chariker L, Shapley R, Young LS (2016) Orientation selectivity from very sparse lgn inputs in a comprehensive model of macaque V1 cortex. *J Neurosci* 36:12368–12384.
3. Sclar G, Freeman RD (1982) Orientation selectivity in the cat's striate cortex is invariant with stimulus contrast. *Exp Brain Res* 46:457–461.
4. Skottun BC, Bradley A, Sclar G, Ohzawa I, Freeman RD (1987) The effects of contrast on visual orientation and spatial frequency discrimination: A comparison of single cells and behavior. *J Neurophysiol* 57:773–786.

5. Ben-Yishai R, Bar-Or RL, Sompolinsky H (1995) Theory of orientation tuning in visual cortex. *Proc Natl Acad Sci USA* 92:3844–3848.
6. Troyer TW, Krukowski AE, Miller KD (2002) Lgn input to simple cells and contrast-invariant orientation tuning: An analysis. *J Neurophysiol* 87:2741–2752.
7. Lauritzen TZ, Miller KD (2003) Different roles for simple-cell and complex-cell inhibition in V1. *J Neurosci* 23:10201–10213.
8. Finn IM, Priebe NJ, Ferster D (2007) The emergence of contrast-invariant orientation tuning in simple cells of cat visual cortex. *Neuron* 54:137–152.
9. Nelson S, Toth L, Sheth B, Sur M (1994) Orientation selectivity of cortical neurons during intracellular blockade of inhibition. *Science* 265:774–777.
10. Ferster D, Chung S, Wheat H (1996) Orientation selectivity of thalamic input to simple cells of cat visual cortex. *Nature* 380:249–252.
11. Chung S, Ferster D (1998) Strength and orientation tuning of the thalamic input to simple cells revealed by electrically evoked cortical suppression. *Neuron* 20:1177–1189.
12. Niell CM, Stryker MP (2008) Highly selective receptive fields in mouse visual cortex. *J Neurosci* 28:7520–7536.
13. Li Yt, et al. (2012) Broadening of inhibitory tuning underlies contrast-dependent sharpening of orientation selectivity in mouse visual cortex. *J Neurosci* 32:16466–16477.
14. Long M, Jiang W, Liu D, Yao H (2015) Contrast-dependent orientation discrimination in the mouse. *Sci Rep* 5:15830.
15. Liu Bh, et al. (2010) Intervening inhibition underlies simple-cell receptive field structure in visual cortex. *Nat Neurosci* 13:89–96.
16. Liu Bh, et al. (2011) Broad inhibition sharpens orientation selectivity by expanding input dynamic range in mouse simple cells. *Neuron* 71:542–54.
17. Bock DD, et al. (2011) Network anatomy and in vivo physiology of visual cortical neurons. *Nature* 471:177–182.
18. Ko H, et al. (2011) Functional specificity of local synaptic connections in neocortical networks. *Nature* 473:87–91.
19. Lien AD, Scanziani M (2013) Tuned thalamic excitation is amplified by visual cortical circuits. *Nat Neurosci* 16:1315–1323.
20. Ko H, et al. (2013) The emergence of functional microcircuits in visual cortex. *Nature* 496:96–100.
21. Cossell L, et al. (2015) Functional organization of excitatory synaptic strength in primary visual cortex. *Nature* 518:399–403.
22. Kerlin AM, Andermann ML, Berezovskii VK, Reid RC (2010) Broadly tuned response properties of diverse inhibitory neuron subtypes in mouse visual cortex. *Neuron* 67:858–871.
23. Liu Bh, et al. (2009) Visual receptive field structure of cortical inhibitory neurons revealed by two-photon imaging guided recording. *J Neurosci* 29:10520–10532.
24. Jin J, Wang Y, Swadlow HA, Alonso JM (2011) Population receptive fields of on and off thalamic inputs to an orientation column in visual cortex. *Nat Neurosci* 14:232–238.
25. Mata ML, Ringach DL (2005) Spatial overlap of on and off subregions and its relation to response modulation ratio in macaque primary visual cortex. *J Neurophysiol* 93:919–928.
26. Ohki K, et al. (2006) Highly ordered arrangement of single neurons in orientation pinwheels. *Nature* 442:925–928.
27. Bonin V, Histed MH, Yurgenson S, Reid RC (2011) Local diversity and fine-scale organization of receptive fields in mouse visual cortex. *J Neurosci* 31:18506–18521.
28. Gilbert CD (1977) Laminar differences in receptive field properties of cells in cat primary visual cortex. *J Physiol* 268:391–421.
29. Ringach DL, Shapley RM, Hawken MJ (2002) Orientation selectivity in macaque V1: Diversity and laminar dependence. *J Neurosci* 22:5639–5651.
30. Frost DO, Caviness VS (1980) Radial organization of thalamic projections to the neocortex in the mouse. *J Comp Neurol* 194:369–393.
31. Stratford K, Tarczy-Hornoch K, Martin K, Bannister N, Jack J (1996) Excitatory synaptic inputs to spiny stellate cells in cat visual cortex. *Nature* 382:258–261.
32. Cruikshank SJ, Urabe H, Nurmikko AV, Connors BW (2010) Supplemental figures from "Pathway-Specific feedforward circuits between Thalamus and neocortex revealed by selective optical stimulation of axons". *Neuron* 65:230–245.
33. Kloc M, Maffei A (2014) Target-specific properties of Thalamocortical synapses onto layer 4 of mouse primary visual cortex. *J Neurosci* 34:15455–15465.
34. Sohya K, Kameyama K, Yanagawa Y, Obata K, Tsumoto T (2007) GABAergic neurons are less selective to stimulus orientation than excitatory neurons in layer II/III of visual cortex, as revealed by in vivo functional Ca2+ imaging in transgenic mice. *J Neurosci* 27:2145–2149.
35. Runyan CA, et al. (2010) Response features of parvalbumin-expressing interneurons suggest precise roles for subtypes of inhibition in visual cortex. *Neuron* 67:847–857.
36. Herculano-Houzel S, Watson C, Paxinos G (2013) Distribution of neurons in functional areas of the mouse cerebral cortex reveals quantitatively different cortical zones. *Front Neuroanat* 7:35.
37. Grubb MS, Thompson ID (2003) Quantitative characterization of visual response properties in the mouse dorsal lateral geniculate nucleus. *J Neurophysiol* 90:3594–3607.
38. Tan AYY, Brown BD, Scholl B, Mohanty D, Priebe NJ (2011) Orientation selectivity of synaptic input to neurons in mouse and cat primary visual cortex. *J Neurosci* 31:12339–12350.
39. Brette R, Gerstner W (2005) Adaptive exponential integrate-and-fire model as an effective description of neuronal activity. *J Neurophysiol* 94:3637–3642.
40. Shelley MJ, Tao L (2001) Efficient and accurate time-stepping schemes for integrate-and-fire neuronal networks. *J Comp Neuro* 11:111–119.
41. Hansel D, van Vreeswijk C (2012) The mechanism of orientation selectivity in primary visual cortex without a functional map. *J Neurosci* 32:4049–4064.
42. Sadeh S, Rotter S (2015) Orientation selectivity in inhibition-dominated networks of spiking neurons: Effect of single neuron properties and network dynamics. *Plos Comput Biol* 11:e1004045.
43. Roy D, et al. (2013) Afferent specificity, feature specific connectivity influence orientation selectivity: A computational study in mouse primary visual cortex. arXiv:1301.0996. Preprint, posted January 6, 2013.
44. Kang K, Shelley M, Sompolinsky H (2003) Mexican hats and pinwheels in visual cortex. *Proc Natl Acad Sci USA* 100:2848–2853.
45. Pattadkal JJ, Mato G, van Vreeswijk C, Priebe NJ, Hansel D (2018) Emergent orientation selectivity from random networks in mouse visual cortex. *Cell Rep* 24:2042–2050.e6.
46. Srinivasan S, Carlo CN, Stevens CF (2015) Predicting visual acuity from the structure of visual cortex. *Proc Natl Acad Sci USA* 112:7815–7820.

PNAS
www.pnas.org

Supplementary Information for

Mechanisms Underlying Contrast-dependent Orientation Selectivity in Mouse V1

Wei P. Dai, Douglas Zhou, David W. McLaughlin and David Cai

Douglas Zhou.
E-mail: zdz@sjtu.edu.cn
David W. McLauglin.
E-mail: david.mclaughlin@nyu.edu

This PDF file includes:

Supplementary text
Figs. S1 to S10
References for SI reference citations

www.pnas.org/cgi/doi/10.1073/pnas.1719044115

Supporting Information Text

Model Setup

The model is made up of two layers. The first layer consists of LGN cells modeled with a linear-nonlinear-Poisson paradigm, and the second layer is populated by V1 neurons that are postsynaptic to the LGN cells in the first layer. The following subsections describe in detail the model setup, external input properties, LGN kernel convolution, LGN to V1 mapping, and intra-cortical connectivity. The source code may be found at *https://github.com/g13/mouseV1*.

LGN layer. The LGN layer in the model is made up of a grid of 16×16 LGN cells, with a uniform spacing of 4.8 degree, covering a visual field of approximately 75×75 degrees square. The input is a drifting sinusoidal wave

$$I(\vec{r}, t) = I_0 \left(1 + \epsilon \sin\left(\frac{\omega}{2\pi} t - \vec{k} \cdot \vec{r}\right)\right), \quad [1]$$

where the temporal frequency $\omega = 4$ Hz, spatial frequency $\vec{k}$ has an amplitude of 0.04 cycle per degree and points to the direction of drift, I_0 is the luminance of the wave, and ϵ is the contrast. The following detailed parameters for each LGN cell are either fitted or directly selected from Grubb and Thompson (1).

1. The center-surround spatial kernel:

$$A(\vec{r}) = \frac{k_c}{\pi \sigma_c^2} \exp\left[-\left(\frac{\vec{r}}{\sigma_c}\right)^2\right] - \frac{k_s}{\pi \sigma_s^2} \exp\left[-\left(\frac{\vec{r}}{\sigma_s}\right)^2\right] \quad [2]$$

where $k_c = 14.8800$ degree^2, $k_s = 14.4340$ degree^2 and $\sigma_c = 5.6100$ degree, $\sigma_s = 16.9800$ degree are the amplitudes and standard deviations (SDs) of the two Gaussian profiles, respectively. The center-surround structure is concentric.

2. The temporal kernel:

$$G(t) = \frac{t^5}{\tau_0^6} \exp\left(-\frac{t}{\tau_0}\right) - \frac{t^5}{\tau_1^6} \exp\left(-\frac{t}{\tau_1}\right) \quad [3]$$

where $\tau_0 = 14$ ms, $\tau_1 = 23.33$ ms, so that the optimal temporal frequency is approximately 4 Hz.

3. The linear response of the ith LGN cell, $L(\vec{r}_i, t)$, is then calculated by convolving the spatiotemporal kernel with the sinusoidal stimulus,

$$L(\vec{r}_i, t) = \int d\tau \int d\vec{r} A(\vec{r} - \vec{r}_i) G(\tau) I(\vec{r}, t - \tau), \quad [4]$$

where $\vec{r}_i$ are the xy-coordinates of the ith node on the LGN grid with a random offset from a normal distribution with mean zero and SD 1.1460 degree.

4. The nonlinearity has the form of a piecewise function:

$$f(x) = \begin{cases} c_1 x^2 + c_2 x^3 & x \leq 41 \\ d_1 \operatorname{arctanh}(d_2 x + d_3) + d_4 & \text{otherwise} \end{cases} \quad [5]$$

where $c_1 = 0.0983$, $c_2 = -0.0016$, $d_1 = 40$, $d_2 = 0.4692$, $d_3 = -9.8598$ and $d_4 = -2.8319$. In addition, the input and output are scaled with 0.0592 and 0.8750, respectively. With $I_0 = 1$, the gain curve has a spontaneous firing rate of 3.24 Hz, a maximum firing rate around 50 Hz, and a half-maximum at 32% contrast (1).

Finally, we use the nonlinear response $f(L)$ as the modulated rate of a Poisson process to generate the spike train of the ith LGN cell projecting to the corresponding V1 neuron. Note that each node on the LGN grid represents one ON and one OFF LGN cells simultaneously. An ON cell has a positive center and negative surround for its spatial kernel, while an OFF cell has the opposite.

LGN to V1 mapping. A patch of 120×72 excitatory neurons and 60×36 inhibitory neurons is located at the center of the simulated visual field covering 35×35 degree^2. The magnification factors are 25 μm per degree vertically and 15 μm per degree horizontally (2).

To connect the V1 neurons with LGN cells, we first define the vertices of the grid as the tentative centers of the V1 neurons' receptive fields (RFs) from LGN input. Then, the sub-centers of ON and OFF subregions (P_{on} and P_{off}) of the RF can be determined by the distance between them, along with the preferred orientation (PO) of the RF. To obtain the distance between the two sub-centers (tentative), we define the normalized distance, D_{norm} as $|P_{on} - P_{off}|/(r_{on} + r_{off})$ (3), whose values are drawn from a Gaussian distribution with mean 0.305 (3) (0.4 for inhibitory neurons) and SD 0.1. r_{on} and r_{off} are the radii along the minor axis of each subregion, which are drawn from the Gaussian distribution with mean 10.5 degree and SD 0.1 degree, for both excitatory and inhibitory neurons. The orientation of the line that connect the two sub-centers is orthogonal to the PO of the neuron, which is drawn from a uniform distribution of orientations, producing a salt-and-pepper distribution. Thus, P_{on} and P_{off} can be solved. Then, we set a pair of ellipses based on the two sub-centers in the visual field for each neuron, as its tentative ON and OFF subregions, as shown in Fig. S1A. Each pair of ellipses share the same orientation along their major axes, the PO. The major radii are determined from the minor radii and the aspect ratios, which are drawn from another Gaussian distribution with a mean of 1.2 and SD 0.012 for the excitatory population; while the ellipses

of each inhibitory neuron are more elongated, with a mean aspect ratio of 1.4 and SD 0.014, in order to have a more prominent contrast-broadening phenomenon for the orientation selectivity (OS) of inhibitory neurons. This amount of elongation is one way to realize the experimental finding that inhibitory neurons receive more than twice the LGN input received by the excitatory neurons (4, 5). However, the assumption that the aspect ratios of inhibitory neurons' RF induced by presynaptic LGN cells is larger than the ones of excitatory neurons is not essential to the model. A case where the LGN input to inhibitory neurons has the same aspect ratio as that of excitatory neurons but with doubled connection strength also gives similar, although not as prominent, contrast-dependent phenomena (Fig. S2).

Finally, the LGN cells that sit inside the boundary of each ellipse are then connected to the corresponding V1 neuron (approximately 15 LGN cells project to one V1 neuron on average), with the ON/OFF nature of each LGN cell determined by the subregion in which it lies. The single LGN cell connection strength to a V1 neuron is 0.09, comparable with the largest cortical excitatory connection strength of 0.1. Note that for this framework of setup to produce complex excitatory neurons in the model, we need to manually preset a percentage (20%) of D_{norm} to 0 (completely overlapped ON and OFF subregions), see details in the subsection *Complex excitatory neurons* in section *Additional Properties of the Model*.

Cortical connections. In our model, the cortical connections are made through presynaptic connection probability density functions (PDFs) in the form of Gaussian functions. The PDF of presynaptic connections to the excitatory neurons is made up of two components: *first*, a Gaussian function of physical distances between the neuron and its presynaptic neurons; *second*, a Gaussian function of the similarity indices (defined in detail below) between the neuron and its presynaptic neurons. The PDF of presynaptic connections to the inhibitory neurons consists of only the first Gaussian component of physical distance. Both Gaussian have zero mean, and their SDs are model parameters used to tweak the profile of connection PDF. Once the Gaussian functions are determined (where the physical distance and the similarity index are the independent variables), the connection probabilities are the direct readout of the Gaussian functions.

The SD of the first Gaussian function, $\sigma^{(d)}_{k_i \to k_j}$, is determined both by the dendritic extent of postsynaptic neuron den_j and the axonic extent of presynaptic neuron axn_i (these extents are approximately half of the largest radii observed in experiments that a typical neuron can extend), where k_i and k_j are the corresponding population (E or I) to which the ith neuron and the jth neuron belong.

$$\sigma^{(d)}_{k_i \to k_j} = \sqrt{2 \log 2} \sqrt{axn_i^2 + den_j^2}, \qquad [6]$$

where axn_i takes the value of 100 μm or 80 μm corresponding to an excitatory or inhibitory presynaptic neuron, and den_j equals 75 μm or 50 μm, corresponding to an excitatory or inhibitory postsynaptic neuron.

For the second Gaussian function, the similarity index between the ith neuron and the jth neuron is defined as $w \times \Gamma_{ij} + (1 - w)\,\Delta\theta$, where the weight $w = 0.5$, Γ_{ij} is the pixel-to-pixel Pearson correlation coefficient of the pairwise RF, and $\Delta\theta$ is the pairwise PO difference normalized to $[-1, 1]$. To calculate the RF correlation, we make a 60×60 mesh of the whole visual field. At each pixel (node on the mesh grid) P, we calculate the normalized correlation between the pairwise spatial RF amplitude $\bar{A}_i\,(P)$ and $\bar{A}_j\,(P)$, where $\bar{A}_p\,(P)\,, p = i, j$ is an abbreviated form of $\Sigma_k A\,(P - \vec{r}_{p,k})$ from Eq. 2. Here $\vec{r}_{p,k}$ denotes the center of the kth LGN cell that connects to the pth V1 neuron. Then, we average over P:

$$\Gamma_{ij} = \left\langle \frac{\left(\bar{A}_i\,(P) - \langle \bar{A}_i \rangle\right)\left(\bar{A}_j\,(P) - \langle \bar{A}_j \rangle\right)}{\sigma\left(\bar{A}_i\right)\sigma\left(\bar{A}_j\right)} \right\rangle, \qquad [7]$$

where $\langle \bar{A}_i \rangle$ and $\langle \bar{A}_j \rangle$, $\sigma\left(\bar{A}_i\right)$ and $\sigma\left(\bar{A}_j\right)$ are the means and SDs of $\bar{A}_i\,(P)$ and $\bar{A}_j\,(P)$, respectively.

The SD of the second Gaussian function of similarity indices, $\sigma_{k_i \to k_j}$, takes 0.6 for $\sigma_{I \to E}$ and 0.5 for $\sigma_{E \to E}$ in Fig. 2 of the main text (k_i and k_j are the corresponding types of the neuron, E or I). For the standard configurations of the model in the main text (Fig. 3B), $\sigma_{I \to E}$ is assigned with additional values of 0.8, 1.0, and ∞ (in this case, neurons connect uniformly across similarity indices), and $\sigma_{E \to E} = 0.65$ is used for the contrast-invariant example discussed in the main text. Note that, for the modified model introduced at the end of SI, the similarity index only includes the RF CC.

This specific setup results in the distribution of presynaptic connections shown in Fig. S1B, C and D for physical distance, PO difference, and RF correlation coefficient, respectively. Note that V1 population's exceptionally large RF size (~ 40 degree) and fairly high neuronal density ($2.9 \times 10^4/\text{mm}^2$, (6)) enable RFs of different neurons to share a very large overlap region within a reasonable distance. Thus, there are sufficient neurons that have similar RFs. Even still, the percentage of highly RF correlated pairs in the entire network is very small, as shown in the background histogram of Fig. S1E, consistent with the experiment (7).

The total presynaptic connection probability to excitatory neurons is around 15% (of all the neurons it can reach within the physical distance). In terms of number of neurons, one excitatory neuron has about 400 presynaptic excitatory neurons and 100 presynaptic inhibitory neurons. The total presynaptic connection probability to inhibitory neurons is around 60%, that is about 1000 presynaptic excitatory neurons and 300 presynaptic inhibitory neurons.

For the $E \to E$ connection strengths, we first fit the EPSP distribution from the experiment (7) by a log-normal distribution with a mean of 0.45 mV and an SD of 1.16 mV. We then draw a number of EPSPs from this distribution, in our case 400 EPSPs. Next, for each excitatory neuron, the highest EPSP it receives is set to be sent from the presynaptic excitatory neuron with the highest similarity index, then the next highest, and so on so forth to match all the EPSPs with similarity indices sequentially. Finally we transform the amplitude of EPSP to the actual strength of synaptic conductance used in the simulation by matching them with the input-output relation of the V1 neuron model described in the next section. There is approximately

40-fold ratio difference between EPSP amplitudes and the corresponding strengths of synaptic conductance. In addition, we have the excitatory neurons that receive the maximum number of LGN inputs (~ 16) reduce their cortical EPSP amplitudes to 60%, while the neurons that receive the minimum number of LGN inputs (~ 10) were given EPSP amplitudes of 100% in order to roughly balance the total excitation received by each excitatory neuron. With these specifications of connections, we have the top 18% most RF correlated pairs providing 50% of the total cortical excitation (Fig. S1E). This quantifies the level of connection bias that excitatory neurons have in the model, towards those that have similar RFs and POs, comparable with the experiment (7).

For other types of connection strengths, only single values are applied, $S_{E\to I} = 0.09$, $S_{I\to E} = 0.021$, $S_{I\to I} = 0.04$. Note that excitatory to inhibitory connection is quite large, as suggested by Bock et al (8). For the modified model, we have $S_{E\to I} = 0.032$, $S_{I\to E} = 0.022$, $S_{I\to I} = 0.031$, and we expand the variety of cortical EPSP amplitudes such that the excitatory neurons that have the maximum number of LGN inputs only receive cortical EPSP with 10% of the original amplitude (the excitatory neurons with the least number of LGN inputs still receive 100%). However, for the model to produce complex excitatory neurons, single-valued $E \to E$ connection strength are to be applied as well, in addition to setting their D_{norm} to zero.

V1 Neuron Model

Each V1 neuron is represented as a conductance-based exponential integrate-and-fire (EIF) point neuron model (9), with frequency adaptation. The adaptation is modeled by a self-inhibitory conductance g_{adap} that only increases when the neuron itself fires. The EIF model is a balanced choice between physiological realism and simulation efficiency. The voltage dynamics of the ith neuron in the kth population is thus governed by:

$$\begin{aligned}\frac{dV_k^i}{dt} =& - g_{L,k}\left(V_k^i - V_L\right) + g_{L,k}\Delta_T \exp\left(\frac{V_k^i - V_T}{\Delta_T}\right)\\ &+ I_{syn,k}^i(t) - g_{adap}^i(t)\left(V_k^i - V_I\right),\\ I_{syn,k}^i(t) =& -\left(g_{E\to k}^i(t) + g_{LGN\to k}^i(t)\right)\left(V_k^i - V_E\right)\\ &- g_{I\to k}^i(t)\left(V_k^i - V_I\right),\end{aligned} \qquad [8]$$

where $k = E$ or I. $g_{L,E} = 50\ \mathrm{s}^{-1}$ and $g_{L,I} = 70\ \mathrm{s}^{-1}$ are the leak conductance of excitatory and inhibitory neurons, respectively. $V_L = 0$, $V_E = 2.8$, $V_I = -0.4$ are the dimensionless reversal potentials. $\Delta_T = 0.4375$ concerns the voltage slope of spike initiation and $V_T = 1$ is the soft threshold, the hard threshold where V_k^i is reset to V_L is set to 4.375. $I_{syn,k}^i$ is the sum of all synaptic currents, where the excitatory ($g_{E\to k}^i$), LGN ($g_{LGN\to k}^i$) and inhibitory ($g_{I\to k}^i$) conductances are summed over all spikes of the corresponding presynaptic neurons, and together with the adaptation conductance g_{adap}^i, they share a common temporal profile:

$$g(t) = s/\left(\tau_d - \tau_r\right)\left(\exp\left(-t/\tau_d\right) - \exp\left(-t/\tau_r\right)\right), \qquad [9]$$

where τ_r and τ_d are the rising and decaying time constant, respectively, and s is the strength of connection. $\tau_r = 1$ ms and $\tau_d = 3$ ms are used for excitatory and LGN conductances, $\tau_r = 5/3$ ms and $\tau_d = 5$ ms are used for inhibitory conductances, whereas the adaptation conductance has larger time constants, $\tau_r = 2$ ms and $\tau_d = 80$ ms. The simulation is performed with modified second-order Runge-Kutta method (10)

For the modified model introduced at the end of SI, we incorporate the thalamocortical depression in the dynamics of $g_{LGN\to k}^i$, such that the dynamics of LGN input conductance further consists of two more variables, as modeled by Varela et al. (11).

$$\begin{aligned} g_{LGN\to k}^i =& g_{LGN\to k}^{i,0} DF\\ \tau_D \frac{dD}{dt} =& 1 - D\\ \tau_F \frac{dF}{dt} =& 1 - F\end{aligned} \qquad [10]$$

where $g_{LGN\to k}^{i,0}$ still possesses the profile from Eq. 9, D is the depressing factor and F is the facilitating factor, both recover to 1.0 with the time constants $\tau_D = 120$ ms and $\tau_F = 20$ ms, respectively. At the time of an incoming LGN spike the factors change accordingly with $D \to Dd$, and $F \to F + f$, here $d = 0.17$ and $f = 0.7$ (12).

In addition to the $1 - CV = \left|\Sigma_j r_j e^{2i\theta}\right| / \Sigma_j r_j$ (CV as circular variance), which is used in the main text to measure the OS, two more descriptive quantities are used here: the orientation selectivity index (OSI),

$$\mathrm{OSI} = \left|R_p - R_o\right| / \left(R_p + R_o\right), \qquad [11]$$

where R_p and R_o denote the firing rate responses at preferred and orthogonal orientation (OO), respectively. The tuning width is the half width at the half height of the fitted tuning curve. To obtain the tuning width, the tuning curve is first fitted to a Von Mises function,

$$f(\theta) = r_o + r_p \exp\left((\cos(2(\theta - \theta_p)) - 1)/\sigma_\theta\right), \qquad [12]$$

where r_p and r_o are the parameters to be fitted for firing rate at PO and OO, respectively, and θ_p is the parameter to be fitted for PO, and σ_θ is the parameter to be fitted for the standard deviation of the Von Mises function. The tuning width so defined is limited by a maximum value of 45 degree. Another fitting method uses a lifted Gaussian function with cutoffs at both ends; this fitted tuning width can exceed 45 degree.

Additional Properties of the Model

In addition to the contrast-dependent OS analyzed in detail in the main text, many other response properties of our model are comparable with experiment, e.g., firing rate levels (Fig. S3, (13–15)), the tuning width distribution (Fig. S4, (13)) and the response modulation $F1/F0$ distribution (Fig. S5, (13)). Moreover, in different configurations, the model is also capable of producing complex excitatory neurons.

Firing rate and inter-spike interval. The firing rate distribution of the excitatory neurons (Fig. S3A) with optimal input orientation has a much longer tail than the inhibitory firing rate distribution (Fig. S3B), which is the result of having a log-normal EPSP distribution and preferential connections to excitatory neurons of similar PO and RF. Because of the finite number of neurons, regardless of the uniformly distributed PO, there are always some neurons that may connect to more neurons of similar PO and RF, thus, promoting their firing rates substantially. The overall level of the firing rates in both populations is comparable to what is found in mouse V1 by the experiments (13–15).

Here, we also provide the inter-spike interval (ISI) probability distributions of our simulation in Fig. S3C and D. However, to the best of our knowledge, experimental results on ISI distributions are lacking so far. This prevents us from performing a quantitative comparison with our simulation results. Nevertheless, the causes of the peak positions in the ISI distributions are discussed as below.

We first consider the ISI probability distribution of excitatory neurons in Fig. S3C whose PO matches the input orientation of a single simulation trial (with multiple periods of drifting sinusoidal wave). The first peak is at 50 ms, which results from the rapid firing near the peak of the sinusoidal wave, the resulting instantaneous firing rate is around 20 Hz. As shown in Fig. S3A, excitatory neurons with mean firing rate at such level only constitute of a small fraction of the population. Thus, the excitatory neurons that only have the first peak in their own ISI distribution must be those who have the highest firing rates. The second peak, at 250 ms, results from the 4 Hz periodic oscillation of the drifting grating stimuli which separate pairs of consecutive spikes by the valley of sinusoidal waves. The remaining peaks at ~ 500 ms and ~ 750 ms are multiples of the period of the input oscillation, indicating neurons with lower firing rate, there are pairs of consecutive spikes occasionally separated by two or more periods of input. Actually most of the excitatory population have two or three peaks in their ISI distribution, since the firing rate distribution of excitatory neurons peaks around ~ 5 Hz matching with the input (Fig. S3A). These peaks that have a larger ISI than 200 ms result from the neurons that lack such clusters as shared by the high firing rate neurons.

On the other hand, the firing rate of the inhibitory neurons is higher and the lowest firing rate is around 10 Hz, therefore, there is nearly no multiple peaks from the influence of the input oscillation (all the ISI peaks in Fig. S3D are within 250 ms). In addition to the high firing rates, the inhibitory to inhibitory connections are strong enough to produce some intrinsic oscillation in the model. As one can observe in the ISI distribution, there are multiple peaks with a period ~ 20 ms, indicating an oscillation around 50 Hz (gamma oscillation) in the inhibitory network. As the multiple peaks in the excitatory ISI distribution are the results of the input oscillation, similarly, the multiple peaks here are caused by this intrinsic oscillation, where there exist pairs of consecutive spikes separated by different multiples of the period of this oscillation. Note that the oscillation frequency is larger than the mean firing rate of the individual inhibitory neurons, thus, most of the inhibitory neurons must have multiple peaks in their own ISI distribution.

Tuning width. In addition to the $1 - CV$ to describe the contrast-dependent OS shown in the main text, here we provide another view from the tuning width, fitted from a lifted Gaussian function with cutoffs at both ends in Fig. S4A and B. The contrast-sharpening effect is apparent in Fig. S4A, since most of the tuning widths are larger at 25% contrast, below the contrast-invariant line; while in Fig. S4B, a clear contrast-broadening effect is shown, since most of the tuning widths are larger at 100% contrast, above the contrast-invariant line. To compare the result of tuning width with experiment (13) and theoretical work (16), we provide the distribution of the tuning width fitted by the Von Mises function (Eq. 12) in Fig. S4C and D. Note that for the inhibitory population, most of the tuning widths cluster at 45 degrees, since that is the maximum allowed by fitting with the Von Mises function. The excitatory neurons' tuning width distribution peaks around 20 degree and agrees well with the previous experimental result (13). Most of the inhibitory neurons in the model lack orientation preferences, thus, a complete comparison of tuning width distribution cannot be made with the previous experiments (13, 17), as they only provided tuning width of the few orientation-selective inhibitory neurons.

F1/F0 distribution. The reproduction of the $F1/F0$ distribution in Fig. S5, especially the peak positions (comparable with the experiment (13)), demonstrates that the model performance is consistent with the the experiment. The model setup is based on the following separate experiments: i) the level of overlap between ON and OFF subregions induced by presynaptic LGN cells (3) in mouse V1, ii) the positive correlation between connection probability, connection strength, and pairwise RF similarity within the excitatory population (7), and iii) strong orientation unspecific connection from excitatory neurons to the inhibitory neurons (8). We point out that due to the above setup, the consistency of F1/F0 distribution between the model result and the experiment is guaranteed.

To elaborate, in a purely feed-forward model, the distribution of D_{norm} between ON and OFF subregions would mostly dictate how $F1/F0$ would distribute. In the mouse case, the largely overlapped ON and OFF subregions induced by presynaptic LGN cells (3) lead to weakly tuned LGN inputs, which imply that the peak of the distribution of either the neurons with $F1/F0 < 1$ (complex) or with $F1/F0 > 1$ (simple) would be quite close to 1 (neither completely untuned nor strongly tuned).

However, the $F1/F0$ distribution of inhibitory neurons at higher contrasts is mostly controlled by the strong cortical excitation (8) impinging on the inhibitory neurons, which dominates the LGN input, as shown in Fig. S6B. Since this cortical excitation is not correlated through RFs or POs, hence it has neither orientation preference nor temporal phase preference, indicating a even more overlapped ON and OFF subregion. Rather, it consists, in a "superposition" of all temporal phases, thus, inhibitory neurons will have a distribution of $F1/F0$ that will peak significantly below one (Fig. S5A) – resulting in "complex" inhibitory neurons.

On the other hand, the excitatory neurons connect preferentially to excitatory neurons that share similar PO and RF and with stronger connection strengths, as suggested by (7). This preferential excitation results in stronger response near the peaks of the ON and OFF subregions. Thus, with the cortical inhibition from the complex inhibitory neurons to pull down both subregions, they are effectively more segregated than the ones with only LGN input, as can be seen in Fig. S6A. Therefore, the excitatory neurons will have a distribution of $F1/F0$ that will peak significantly above one (Fig. S5B). Thus, the excitatory neurons behave linearly as "simple" excitatory neurons.

Complex excitatory neurons. Note that in experiment (18), it is found that L2/3 excitatory neurons exhibit both On and Off subregions, with their spatial arrangement varying from being completely segregated to completely overlapped. If we manually supply some excitatory neurons with completely overlapping ON and OFF subregions induced by presynaptic LGN cells (by presetting D_{norm} to zero), and single-valued excitatory connection strengths (as opposed to the log-normal distribution that neurons with non-zero D_{norm} have), we are able to produce a more realistic bimodal $F1/F0$ distribution of excitatory neurons (Fig. S7C), with both the complex and simple excitatory neurons exhibiting contrast-sharpening OS (Fig. S7A and B). Note that in the original setup of D_{norm} distribution, we only follow the experimental observation of the distribution of D_{norm} in layer 4 (3), thus the experimentally observed percentage (20%) of complex excitatory neurons cannot be generated. However, it is layer 2/3 where most complex excitatory neurons are found (13) and these neurons possess almost completely overlapped ON and OFF subregions. In addition, it is shown that V1 neurons that have more overlapped ON and OFF subregions are more likely to be complex neurons (18).

Details of the Mechanisms Underlying Contrast Dependencies

The three primary mechanisms introduced in the main text – the preferential excitation and the high level of feedback inhibition within the excitatory population, and the strong orientation-unspecific cortical excitation to the inhibitory population – are closely related and work with each other cooperatively to produce the contrast dependencies. One of the intricacies induced by the cooperation among the primary mechanisms is well demonstrated in the difference shown between Fig. 3B and D in the main text, where the contrast-broadening of $g_{I\to E}$, contributes to the contrast-sharpening of excitatory neurons in the standard configuration (Fig. 3B in the main text), but fails to do so in the single-valued EPSP configuration (Fig. 3D in the main text), since in the latter case, the reduction of $1-\mathrm{CV}$ at lower contrast in Fig. 3D in the main text is comparable with the reduction at higher contrast as $\sigma_{I\to E}$ decreases, rendering only the effect of residing along the contrast-invariant line rather than moving away.

To understand how all three primary mechanisms relate to the contrast-broadening of $g_{I\to E}$ in determining the excitatory neurons' contrast-dependent response properties, we study the input conductances and firing rates with respect to contrast and $\sigma_{I\to E}$. Fig. S8A plots the ratio of inhibitory conductance $g_{I\to E}$ to the total excitatory conductance $(g_{E\to E} + g_{LGN\to E})$ for the standard configuration. It is surprising that the ratio is almost constant at PO with different $\sigma_{I\to E}$, because with a smaller $\sigma_{I\to E}$, more inhibitory neurons of similar POs are connected. Thus, one would expect the numerator, $g_{I\to E}$, to increase with smaller $\sigma_{I\to E}$, and the denominator to decrease with $g_{E\to E}$ as the increasing inhibition lowers the excitatory firing rate (Fig. S8B). Nevertheless, Fig. S8B shows that the inhibitory firing rates themselves decrease with smaller $\sigma_{I\to E}$, indicating a decreased numerator.

To see the underlying cause of the decrease in $g_{I\to E}$, we separate the two sources that drive the inhibitory firing rate – excitation from the LGN and from the cortex. We can see in Fig. S8C that the cortical excitation (blue) induces $\sim 70\%$ (red asterisks) of the total inhibition to excitatory neurons in terms of $g_{I\to E}$. This result shows that, with smaller $\sigma_{I\to E}$, the decrease in excitatory firing rate causes a much larger decrease in $g_{I\to E}$ induced by cortical excitation than the increase in the $g_{I\to E}$ at PO induced by LGN excitation (Fig. S8C). This indicates the importance of the preferential excitation, which elicits a high excitatory firing rate to drive the inhibitory neurons that, in turn, provide the strong cortical feedback inhibition to the excitatory neurons.

Meanwhile at the OO, at both contrasts, the ratio decreases with smaller $\sigma_{I\to E}$ as expected (Fig. S8A), which results in higher excitatory firing rates, thus reducing the overall $1-\mathrm{CV}$ at both contrasts (Fig. 3B in the main text). However, under higher contrast, the feedback inhibition is already much stronger (compare the ratio across contrasts in Fig. S8A); thus, the marginally lesser inhibitory effect caused by smaller $\sigma_{I\to E}$ (at each contrast) is less effective to raise the firing rate at OO than at lower contrast, and consequently, $1-\mathrm{CV}$ is not reduced as much. Therefore, the contrast-broadening of $g_{I\to E}$ contributes to the contrast-sharpening of excitatory neurons in the standard configuration by reducing $1-\mathrm{CV}$ more at lower contrast.

Thus, in the case of single-valued EPSP (Fig. 3D in the main text), without the strong preferential cortical excitation to trigger the feedback inhibition, the reductions of $1-\mathrm{CV}$ are comparable at both contrasts. This explains why the effect of contrast-broadening of $g_{I\to E}$ for contrast-sharpening of the OS in excitatory neurons is much less effective in this case compared with the standard case (Fig. 3B in the main text). This comparison demonstrates the importance of cooperation among all three primary mechanisms and clarifies in some way, their impact on the effectiveness of the secondary mechanism and the details of the contrast-dependent OS.

Simulation-assisted Analysis

An analytical way to gain insight into the model's simulation results is to examine the "slaving potential" (V_s), to which the membrane potential relaxes on a time scale set by the total conductance g_{tot}. Both the definition of the slaving potential V_s, and that the membrane potential relaxes to it, are immediately apparent from the standard integrate-and-fire model, which can be written in the form

$$\frac{dV}{dt} = -g_{tot}\left(V - V_s\right) \qquad [13]$$

where

$$\begin{aligned} g_{tot} &= g_E + g_I + g_L + g_{LGN}, \\ V_s &= \frac{\left(g_E + g_{LGN}\right)V_E + g_I V_I + g_L V_L}{g_{tot}}. \end{aligned} \qquad [14]$$

Here we directly adapt this formula to EIF model from Eq. 8, neglecting its exponential term since its effect is over very short time windows of the spike duration (~ 2 ms), and its adaptation conductance for simplification. In these units, the relaxation time constant is the reciprocal of the total conductance g_{tot}, which, for mouse V1, has $g_L \sim 50\ \mathrm{s}^{-1}$ as its lower bound. g_{tot} itself can exceed $200\ \mathrm{s}^{-1}$ at higher contrast. This implies that the temporal profile of the slaving potential $V_s(t)$ can accurately follow the temporal profile of the membrane potential $V(t)$ over time scales up to ~ 10 ms.

Contrast dependencies of OS in slaving potential. As clearly shown in Fig. S9A, the excitatory (inhibitory) neuron's slaving potential sharpens (broadens) with increasing contrast, where the sum of response modulation F0 and F1 components of the slaving potential, V_s^{F0+F1}, is used to emphasize on the temporal modulation. Both the "true" form of V_s^{F0+F1} (as calculated from V_s^{F0+F1} averaged from each time-point) on the left panels of Fig. S9A, and the "pseudo" form of V_s^{F0+F1} (as calculated from pre-averaged conductances) on the right panels of Fig. S9A show very similar contrast dependencies both in terms of $1-\mathrm{CV}$ and OSI in the upper panels and lower panels of Fig. S9A, respectively. Thus, the contrast dependencies of the slaving potential, and hence the membrane potential, are similar to those of the firing rates, such that we can actually infer the properties of firing rate OS from V_s^{F0+F1} through simple arithmetics of data collected from simulation. From here on, we will focus on the discussion about the slaving potential in the "pseudo" form as V_s^{F0+F1} instead of the "true" form or plain V_s.

Dissect conductance contributions. In addition, we can also use Eq. 14 in terms of the contributions from conductances to V_s to reveal mechanisms underlying the contrast-sharpening and contrast-broadening phenomena. First, we rewrite Eq. 14 in the form:

$$V_s = \frac{g_E + g_{LGN}}{g_{tot}}V_E + \frac{g_L}{g_{tot}}V_L + \frac{g_I}{g_{tot}}V_I, \qquad [15]$$

such that the value of V_s^{F0+F1} can be seen as being pulled from V_L toward V_E or V_I by excitation or inhibition, respectively. Thus, by calculating how different conductances contribute to the change of OS of V_s^{F0+F1} from Eq. 15 (using conductances obtained from simulation data), one can gain insight into the mechanisms that produce contrast-sharpening or contrast-broadening OS.

Even the detailed changes of OS that result from the change of $\sigma_{I\to E}$, which directly relates to the contrast-broadening of $g_{I\to E}$ (the secondary mechanism in the model), can be captured by this approach, as demonstrated in Fig. S9B. Comparing the phenomena associated with contrast-broadening of $g_{I\to E}$ as described previously in the section "*Details of the Mechanisms Underlying Contrast Dependencies*" with what is shown here in Fig. S9B, one can find that, with $\sigma_{I\to E}$ decreasing from ∞ to 0.6, the decrease of excitation at PO (solid red), the increase of excitation at OO (dotted red), the decrease of inhibition (blue) at both orientations. All these give rise to a decreased OSI for V_s^{F0+F1} of excitatory neuron, which can be readily seen from the increase of V_s^{F0+F1} at OO (dotted black) and the decrease of V_s^{F0+F1} at PO (solid black), all the features that we show in the previous section are captured here – thus confirming the interactions among the mechanisms underlying the contrast dependencies that described in the main text by the firing rates are the same as described here by the slaving potentials.

With the averaged conductance data from the simulation, by using Eq. 14, one can also infer qualitative changes of the OS of V_s^{F0+F1} that result from the change of strength in one of the conductances. To predict the change of direction (sharpening or broadening) of the OS, one simply applies the presumed change in the individual conductances in Eq. 14 and assumes that other conductances are held constant (ignoring the feedback effects). Thus, the V_s^{F0+F1} at PO and OO can be calculated from Eq. 14 and then its OSI can be obtained from Eq. 11. For example, if we increase $\sigma_{I\to E}$, which broadens the $g_{I\to E}$ then the inhibitory conductance will decrease at PO and increase at OO, relatively. Thus, at PO, since V_I is negative the numerator will increase with decreased inhibitory conductance, while the denominator decreases – resulting in an increase of V_s^{F0+F1} at PO. At OO, the opposite occurs, therefore V_s^{F0+F1} is decreased at OO. Taken together, it follows that the OSI of V_s^{F0+F1}

increases and we arrives at a qualitative prediction that the increase of $\sigma_{I\to E}$ leads to the sharpening of OS in the excitatory neurons, consistent with the result from Fig. 3B in the main text.

In summary, we have illustrated that by calculating the OS of the V_s^{F0+F1} with regard to contrast, one can infer the corresponding contrast-related OS change in firing rates, and that one can gain some insight of how the OS changes with respect to changes of contribution from different conductances.

Modified Model with Synaptic Depression for LGN Inputs

Here we describe an modified model, which differs from the model described in the main text in three ways: i) It includes synaptic depression for the LGN inputs (see Eq. 10); ii) The similarity index describing the preferential coupling is based solely on similarities of RFs, with the difference of orientation preference dropped; iii) It has slightly different coupling strengths as described above in subsection *Cortical connections*. With these three changes, the modified model gives a more realistic firing rate at low contrast (Fig. S10A), as well as an OS distribution of $1 - CV$ (Fig. S10B) that better agrees with the measured values of OS (3, 13, 14, 19). Meanwhile, the contrast sharpened (broadened) OS of excitatory (inhibitory) neurons still holds, as shown in Fig. S10B and C.

When we compare Fig. S10D, E and F with the Fig. 3B, C and D in the main text (noticing the different range of $1 - CV$ values), we see that the major mechanisms underlying the contrast-sharpening, i.e., the strong feedback inhibition and the connection preference of log-normal distribution of EPSPs, still hold for the modified model. Other population properties such as the F1/F0 distribution as shown in Fig. S10G and H, also agree with those of of the original model and with the experimental measurements (13).

However, the contrast-broadening of $g_{I\to E}$ is significantly weakened in this modified model, as shown in Fig. S10I. (One can also confirm this weakening from Fig. S10D, since the enhancement of contrast-sharpening of OS in the excitatory population is not as significant as that in the main text.) This weakened contrast-broadening of $g_{I\to E}$ is due to the relatively high cortical excitation to the inhibitory neurons at low contrast, caused by the higher excitatory firing rate (since our gain curve now has a higher firing rate at low contrast). Therefore, the inhibitory neurons' tuning curves are not sharp enough at low contrast to mediate a strong effect of contrast-broadened $g_{I\to E}$. Thus, this weakened contrast-broadening of $g_{I\to E}$ is a compromise for a more realistic gain curve and OS in the modified model.

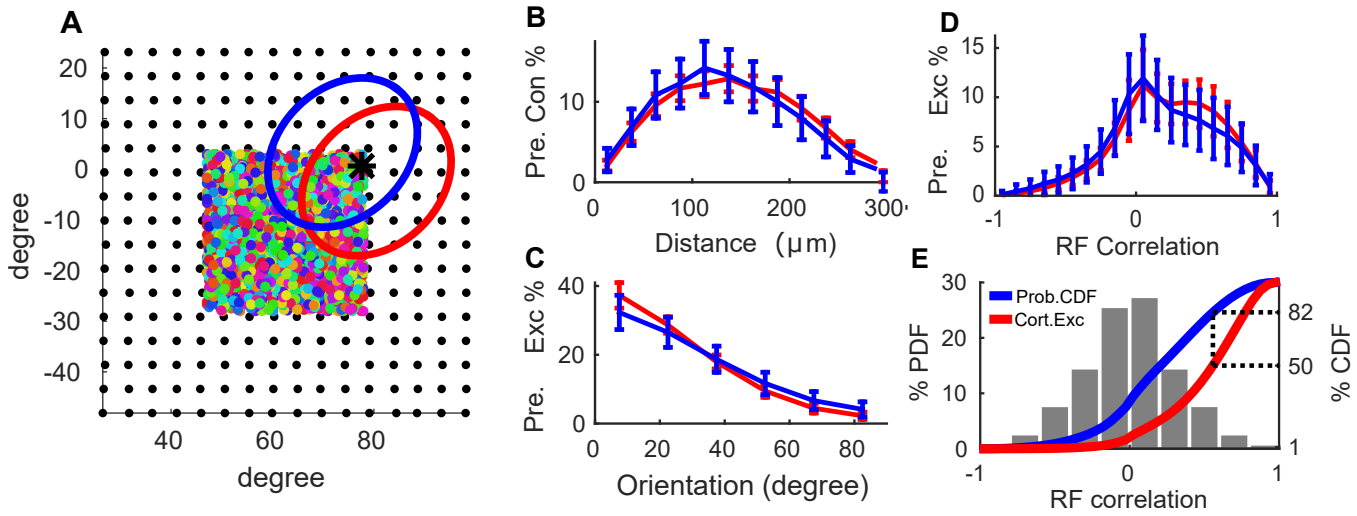

Fig. S1. Simulation Setup. **A**. Layout of LGN cells in black dots, and a patch of V1 neurons in colored dots, where different color indicates different PO. An example of paired ellipses for the ON (red) and OFF (blue) subregions of a V1 neuron (black asterisk) is shown. Note that the total size of the visual field for the LGN patch is larger than the total size of the visual field for the V1 patch, ensuring that all V1 neurons receive a sufficient amount of LGN input. **B**. Percentage of cortical presynaptic connections over radial distance to a postsynaptic V1 neuron, blue for inhibitory postsynaptic neurons and red for excitatory postsynaptic neurons, averaged over the population. **C**. Percentage of excitatory(red) and inhibitory(blue) presynaptic connections to excitatory neurons over difference of PO. **D**. Percentage of cortical presynaptic connections over RF correlation coefficient, using the same color legend as in C. The error bars in **B**, **C** and **D** indicate SD. **E**.Cumulative distribution function (CDF) of cortical presynaptic connections (blue) and cumulative cortical excitation (red), with the top 18% most correlated pairs in RF accounting for 50% cortical excitation indicated by the dotted lines; the histogram of pairwise RF correlations between the excitatory neurons is shown in the background.

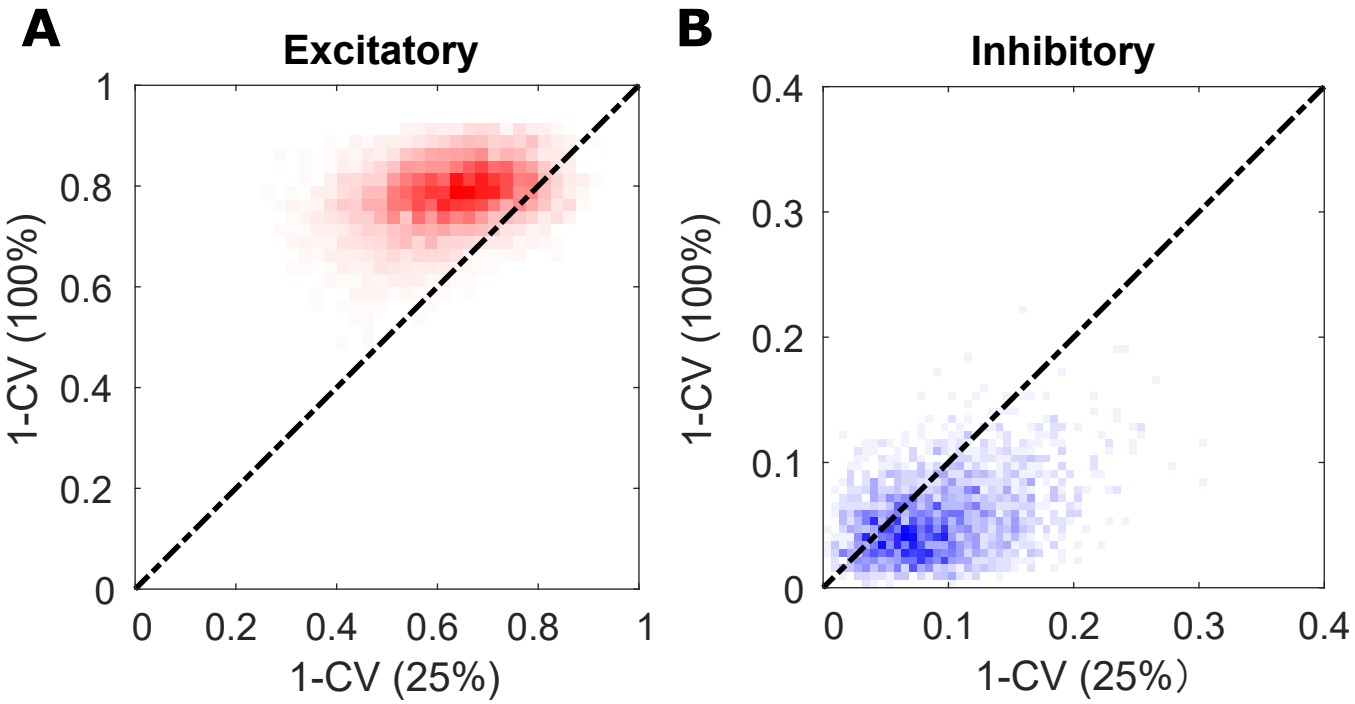

Fig. S2. Contrast dependent OS. Heatmap of $1 - CV$ values of excitatory and inhibitory neurons' tuning curves at 100% contrast versus at 25% contrast, the dotted lines indicate contrast invariance, the same shape and number of LGN input are used for both excitatory and inhibitory neurons in **A** and **B**, but with connection strength on the inhibitory neurons doubled.

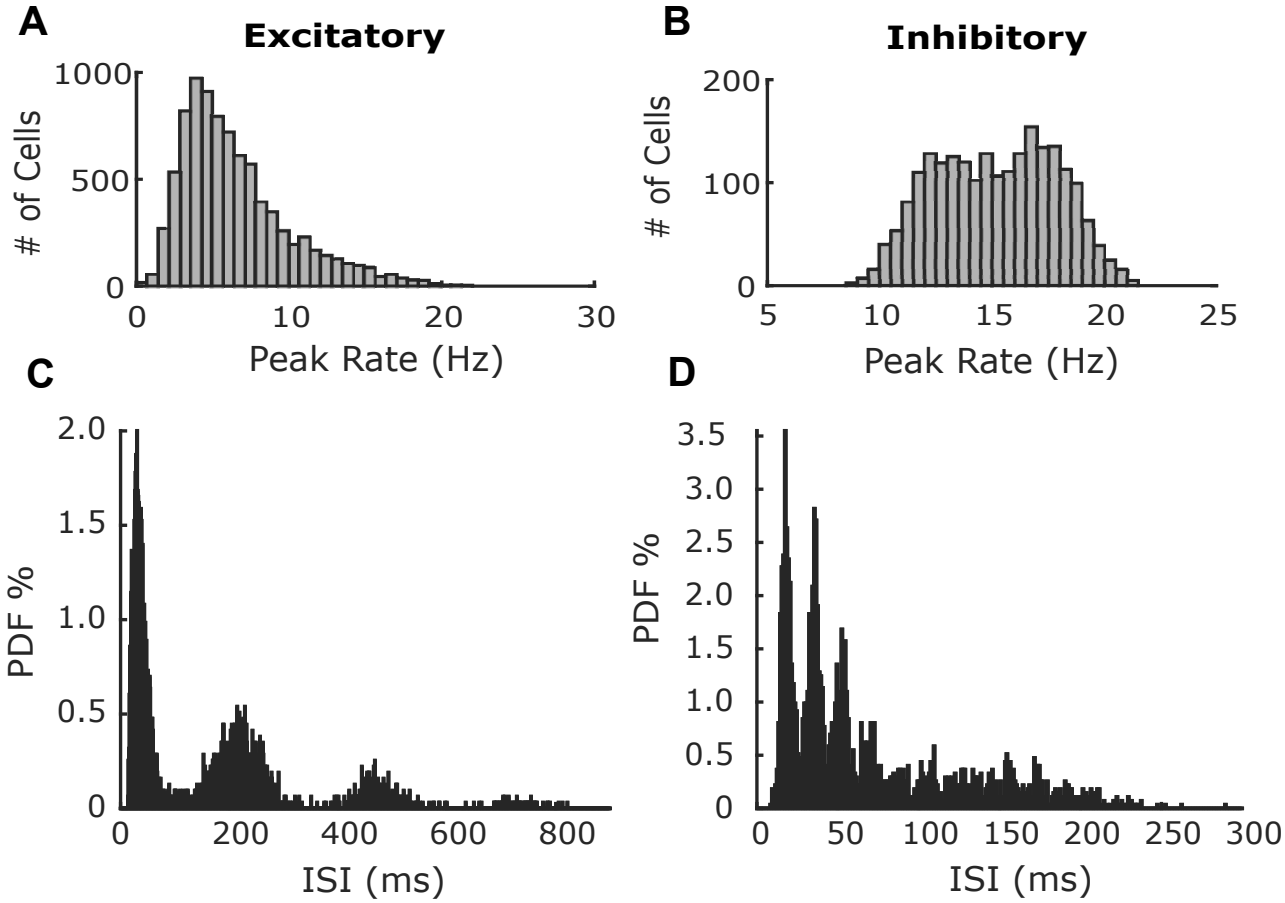

Fig. S3. Firing rate and ISI distribution. The firing rate distribution in **A** and **B** are produced with neurons' firing rate at their PO. The ISI probability distribution in **C** and **D** only include the neurons whose POs match with the input orientation. Only one of the input orientations is used (single trial) to produce the data, but since the PO is uniformly distributed, groups of neurons that have other PO should have similar ISI probability distributions. ISIs are calculated for spike pairs of each neuron, then binned, normalized for each neuron and finally, averaged over all the chosen neurons. **A**. Optimal firing rate distribution of the excitatory population. **B**. Optimal firing rate distribution of the inhibitory population. **C**. ISI probability distribution for the neurons in the excitatory population whose POs match with the input orientation of the trial. **D**. ISI probability distribution for the neurons in the inhibitory population whose POs match with the input orientation of the trial.

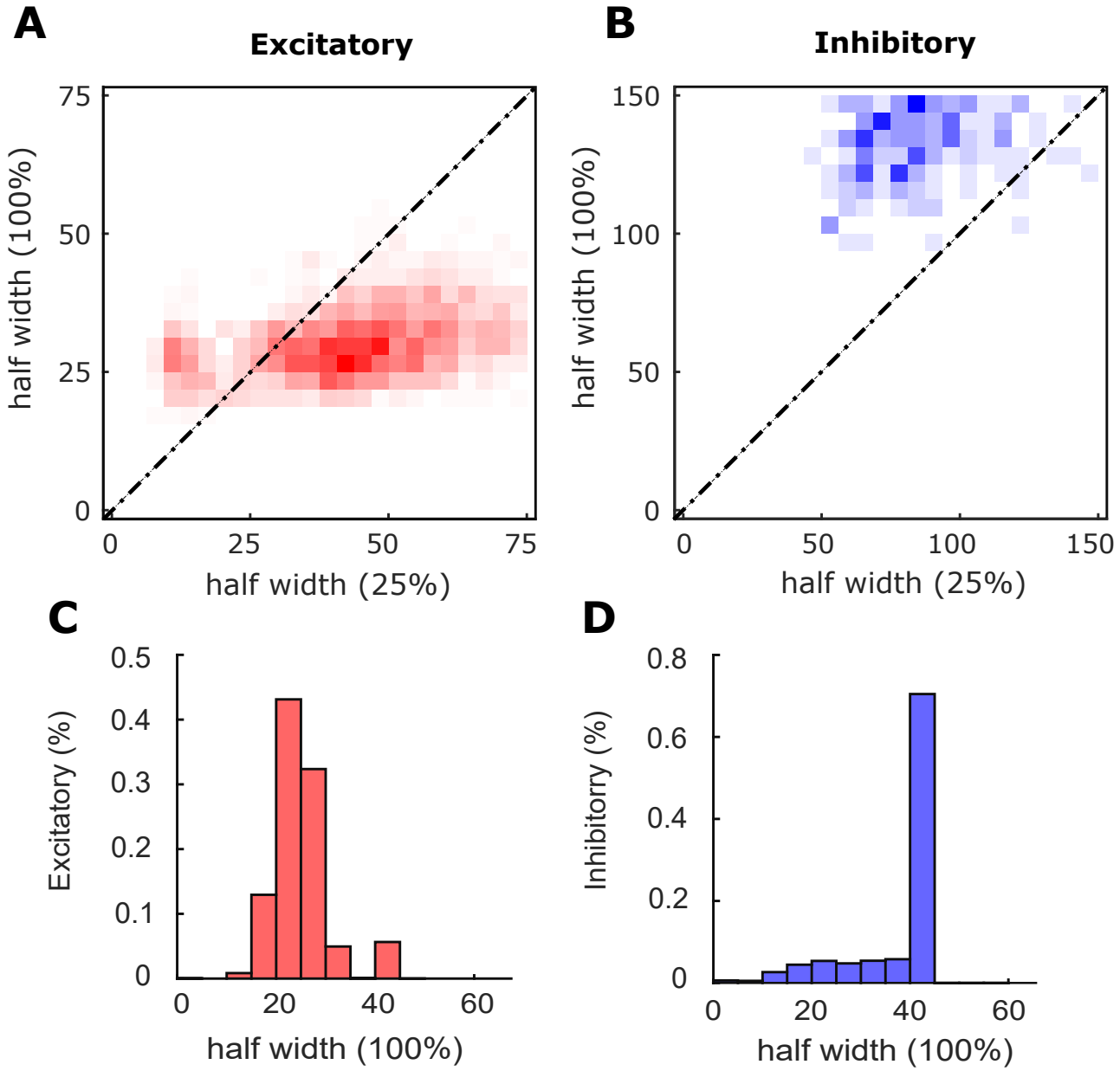

Fig. S4. Tuning width. **A** and **B** use the tuning width fitted by the Gaussian function with cutoffs at both ends; tuning width in **C** and **D** are derived from the tuning curves fitted by the Von Mises function (Eq. 12). **A** The tuning width of excitatory population at 25% contrast versus 100% contrast, where the black dotted line is the contrast-invariant line. **B** The tuning width of inhibitory population at 25% contrast versus 100% contrast. **C** The distribution of excitatory tuning widths at 100% contrast. **D** The distribution of inhibitory tuning widths at 100% contrast.

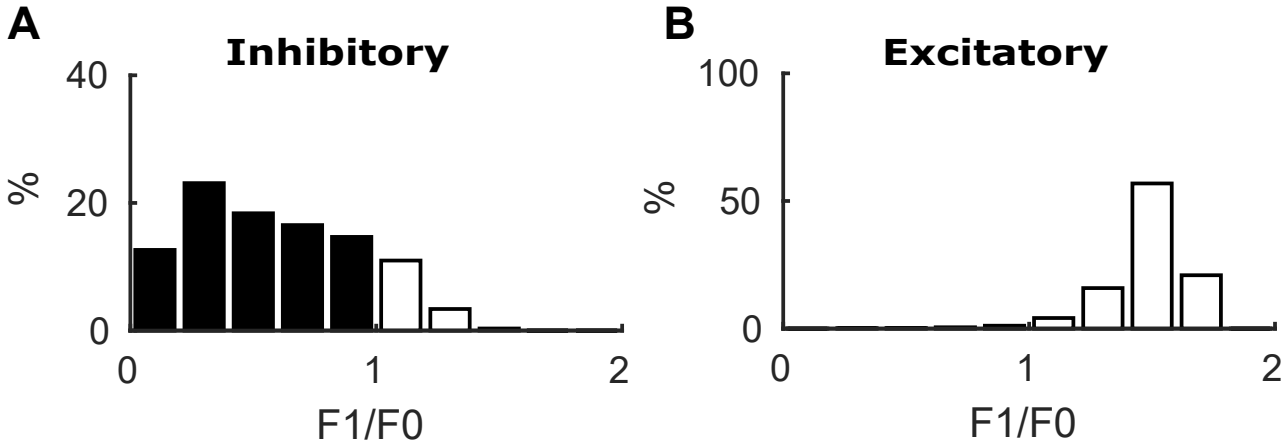

Fig. S5. F1/F0 distribution. Both of the sub-figures are produced with external input at PO for each neuron in the corresponding population. **A**. F1/F0 distribution for inhibitory neurons. **B**. F1/F0 distribution for excitatory neurons.

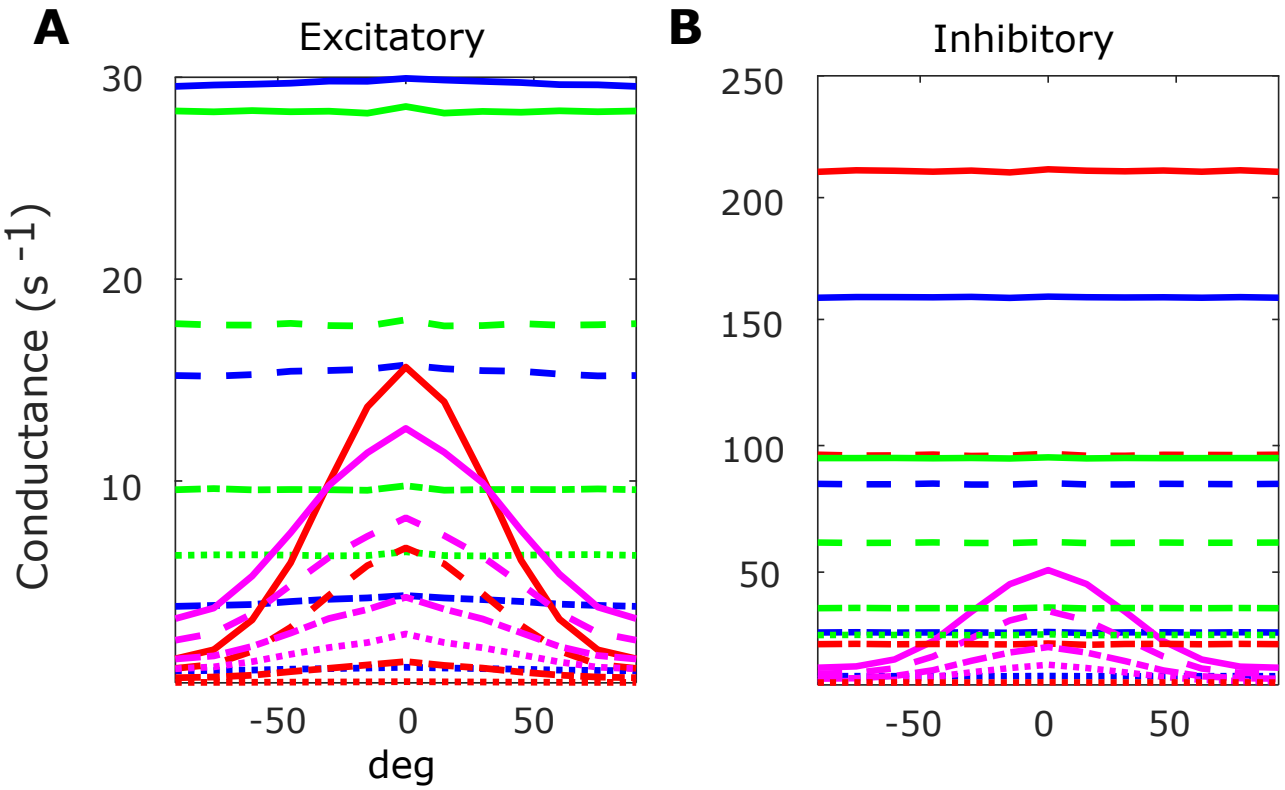

Fig. S6. Conductance Tuning Curve. 12.5%, 25%, 50% and 100% contrast tuning curves are plotted in dotted, dotted-dash, dashed, and solid lines, respectively. Excitatory conductances are in red, inhibitory conductances in blue, LGN conductances in green and the F1 component of LGN conductance in magenta. The tuning curves are averaged over the corresponding population. **A**. Conductance tuning curves of excitatory population. **B**. Conductance tuning curves of inhibitory population.

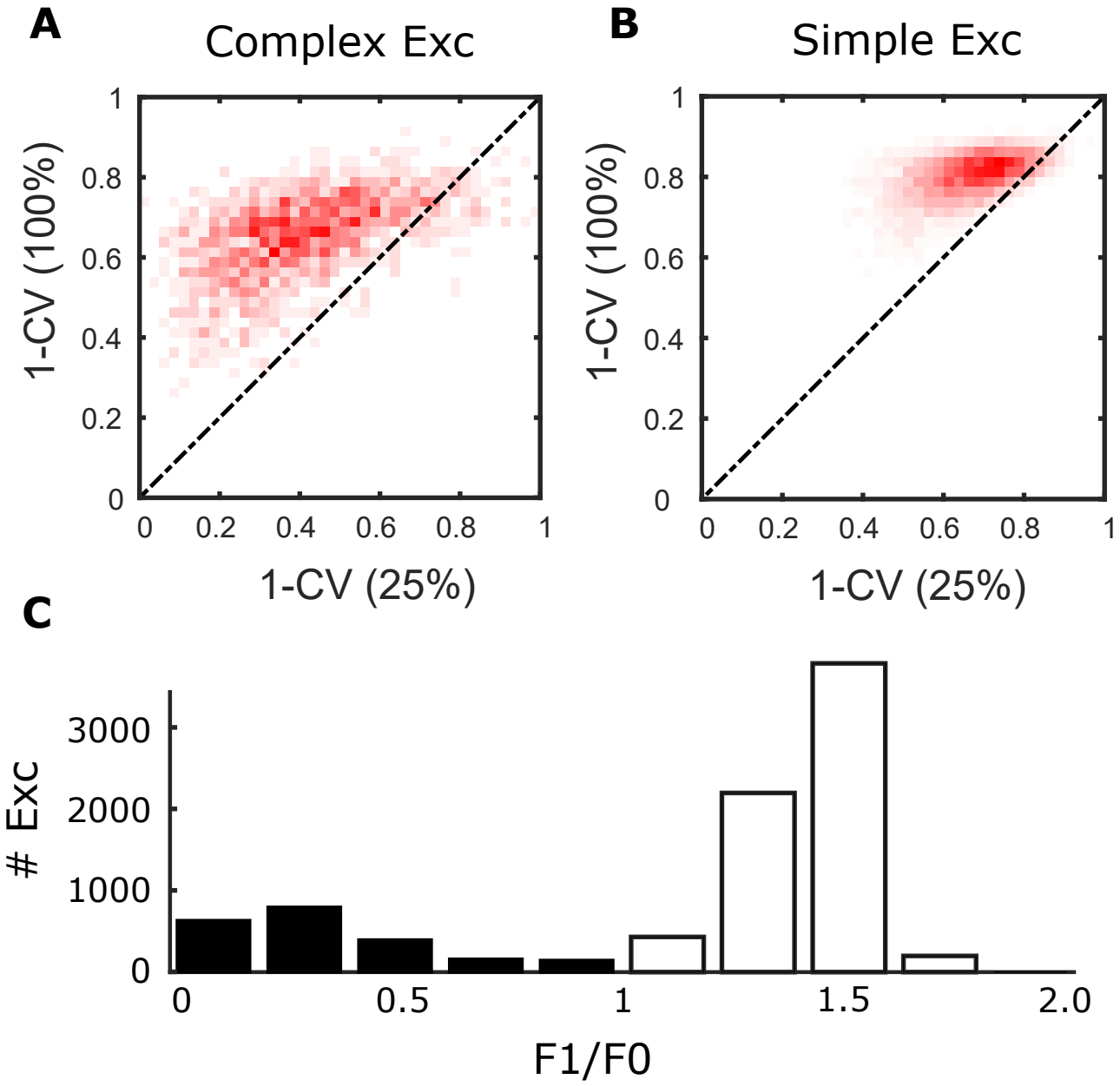

Fig. S7. Simulation results including complex excitatory neurons. The adjustment of completely overlapped ON and OFF subregions configuration for producing complex excitatory neurons. **A** and **B**. Heatmap of $1 - CV$ values of complex and simple excitatory neurons' tuning curves at 100% contrast versus at 25% contrast, the dotted lines indicate contrast invariance. Population of complex excitatory neurons are shown in **A**; Population of simple excitatory neurons are shown in **B**. **C**. $F1/F0$ distribution of the excitatory population, simple excitatory neurons are those with $F1/F0$ value larger than one, and complex excitatory neurons have $F1/F0$ values that are smaller than one.

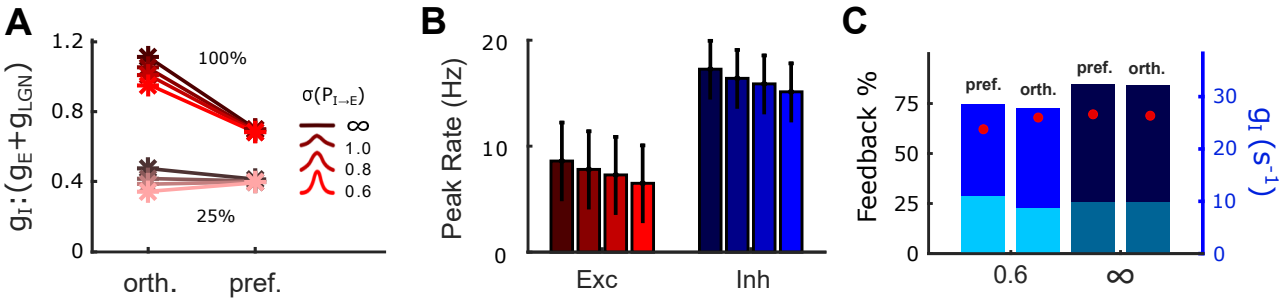

Fig. S8. Mechanistic Analysis. **A**. $g_I/(g_E + g_{LGN})$ ratio for contrast 25% and 100% at PO and OO in excitatory population with 25% contrast shown in less saturated red colors. **B**. Firing rates at PO with 100% contrasts. The legend of excitatory firing rates follows **A**, while the darkness in blue indicate inhibitory firing rates with different $\sigma_{I\to E}$, as in red. Error bars indicate SDs. **C**. Cortical inhibition to excitatory population with $\sigma_{I\to E} = 0.6$ and ∞. Red dots give the percentage of feedback inhibition in the total inhibition (left y-axis); magnitudes of feed-forward inhibition g_I in cyan and feedback inhibition in blue (right y-axis) are stacked together. The feed-forward inhibition is obtained by simulation with the same parameters but without $E \to I$ connections.

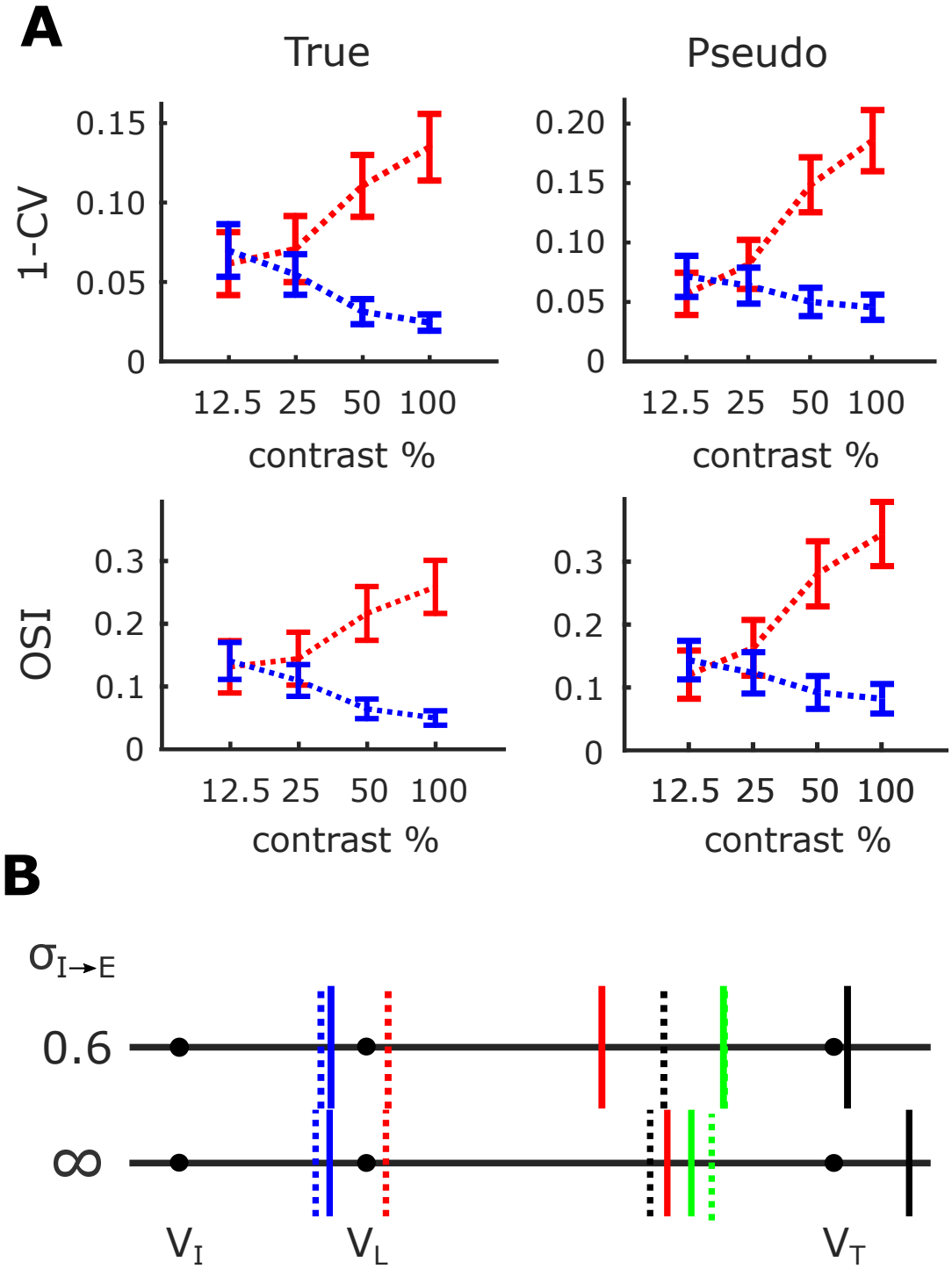

Fig. S9. OS of $\mathbf{V_s}$. **A**. The upper panels show the $1 - CV$ of the tuning curve of V_s^{F0+F1} while the lower ones show the result from the OSI of V_s^{F0+F1}. The two subfigures on the left are calculated from the true V_s at each time point, while the two subfigures on the right use the pseudo V_s^{F0+F1}, which is calculated from pre-averaged conductances by Eq. 15. The OSI and $1 - CV$ of excitatory population are given in red lines and those of inhibitory population are given in blue. **B**. Two axes that show the slaving potential and the contributions from conductances, with $\sigma_{I\to E} = 0.6$ and ∞ are shown. $V_I = -0.4$, $V_L = 0.0$ and $V_T = 1.0$ are shown in black dots. The contributions from inhibitory conductance (blue), $F0 + F1$ components of excitatory conductance (red) and $F0 + F1$ components of LGN conductance (green) at PO are shown in solid lines, while those at OO are shown in dotted lines. The pseudo V_s^{F0+F1} calculated from them are shown in black lines. The error bars in both subfigures indicate the corresponding SDs.

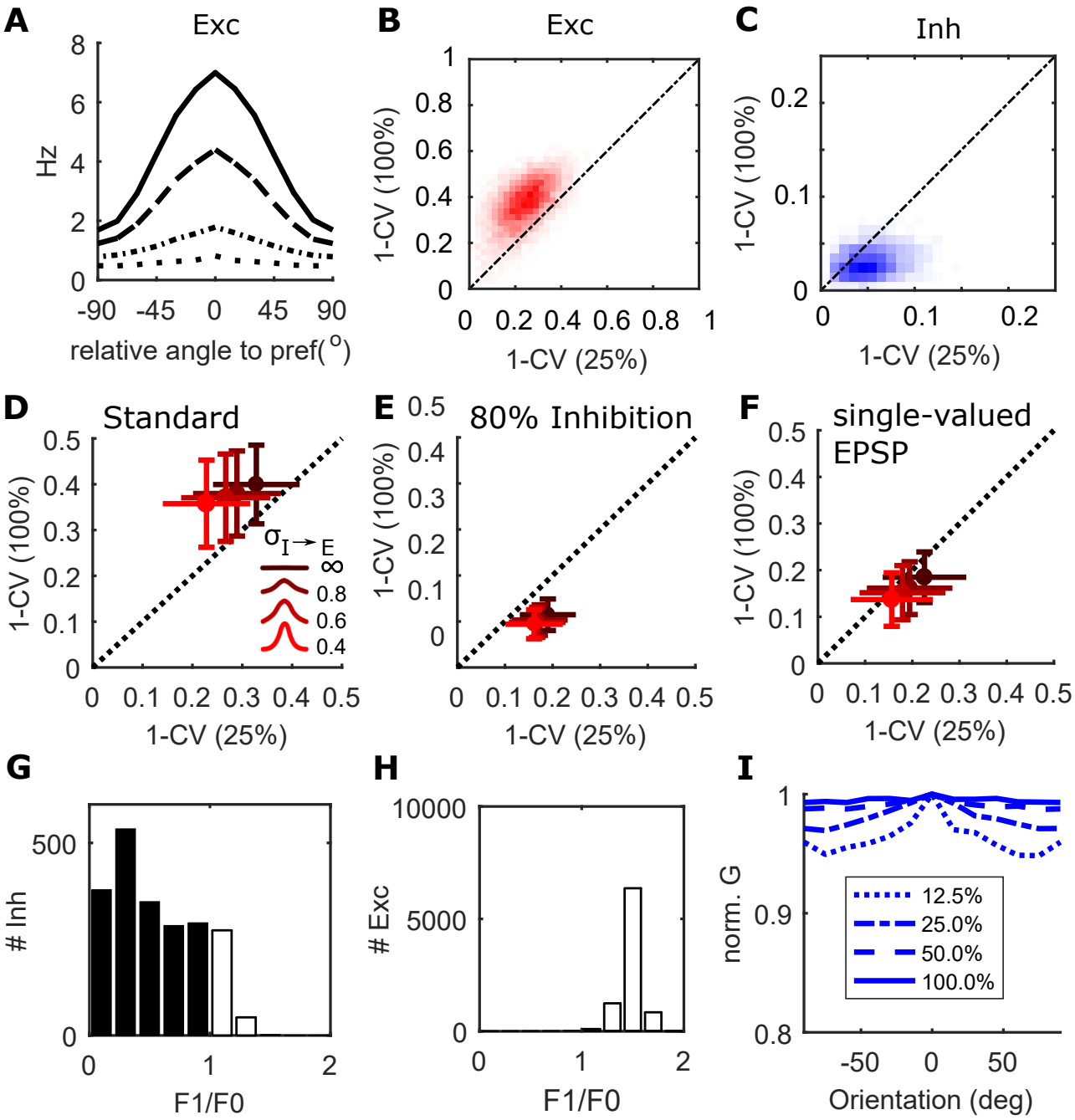

Fig. S10. Results of the modified model. A. Population averaged and aligned tuning curve for the excitatory population. Tuning curves of 12.5%, 25%, 50% and 100% contrasts are in dotted, dot-dashed, dashed and solid lines, respectively. **B**. Heatmap of $1 - CV$ distribution for excitatory population. **C**. Heatmap of $1 - CV$ distribution for inhibitory population. **D**. $1 -$ CV value of the firing rate tuning curves for excitatory populations at 100% contrast versus at 25% contrast, with the same standard parameters used as in **B**, except the SD of $I \to E$ connections, $\sigma_{I\to E} = 0.4, 0.6, 0.8, \infty$, as shown in the legend (0.4 is used for **B**). SDs along both axes are shown by the error bars. **E**. Same as **D**, but with 80% cortical inhibition in excitatory neurons. Connection strengths are adjusted correspondingly. **F**. Same as **D**, but with single-valued EPSP. **G**. F1/F0 distribution for inhibitory neurons. **H**. F1/F0 distribution for excitatory neurons. **I**. Population averaged, aligned and normalized inhibitory conductance of excitatory neurons, notice that the y-axis starts at 0.8.

References

1. Grubb MS, Thompson ID (2003) Quantitative characterization of visual response properties in the mouse dorsal lateral geniculate nucleus. *J Neurophysiol* 90(6):3594–3607.
2. Schuett S, Bonhoeffer T, Hübener M (2002) Mapping retinotopic structure in mouse visual cortex with optical imaging. *Journal of Neuroscience* 22(15):6549–6559.
3. Lien AD, Scanziani M (2013) Tuned thalamic excitation is amplified by visual cortical circuits. *Nat Neurosci* 16(9):1315–1323.
4. Cruikshank SJ, Urabe H, Nurmikko AV, Connors BW (2010) Supplemental Figures from "Pathway-Specific Feedforward Circuits between Thalamus and Neocortex Revealed by Selective Optical Stimulation of Axons". *Neuron* 65(2):230–245.
5. Kloc M, Maffei A (2014) Target-Specific Properties of Thalamocortical Synapses onto Layer 4 of Mouse Primary Visual Cortex. *J Neurosci* 34(46):15455–65.
6. Herculano-Houzel S, Watson C, Paxinos G (2013) Distribution of neurons in functional areas of the mouse cerebral cortex reveals quantitatively different cortical zones. *Frontiers in neuroanatomy* 7(October):35.
7. Cossell L, et al. (2015) Functional organization of excitatory synaptic strength in primary visual cortex. *Nature* 518(7539):399.
8. Bock DD, et al. (2011) Network anatomy and in vivo physiology of visual cortical neurons. *Nature* 471(7337):177–182.
9. Brette R, Gerstner W (2005) Adaptive exponential integrate-and-fire model as an effective description of neuronal activity. *J Neurophysiol* 94(5):3637–3642.
10. Shelley MJ, Tao L (2001) Efficient and accurate time-stepping schemes for integrate-and-fire neuronal networks. *J Comp Neuro* 11(2):111–119.
11. Varela JA, et al. (1997) A quantitative description of short-term plasticity at excitatory synapses in layer 2/3 of rat primary visual cortex. *Journal of Neuroscience* 17(20):7926–7940.
12. Banitt Y, Martin KA, Segev I (2007) A biologically realistic model of contrast invariant orientation tuning by thalamocortical synaptic depression. *Journal of Neuroscience* 27(38):10230–10239.
13. Niell CM, Stryker MP (2008) Highly selective receptive fields in mouse visual cortex. *J Neurosci* 28(30):7520–7536.
14. Li Yt, et al. (2012) Broadening of inhibitory tuning underlies contrast-dependent sharpening of orientation selectivity in mouse visual cortex. *J Neurosci* 32(46):16466–16477.
15. Long M, Jiang W, Liu D, Yao H (2015) Contrast-dependent orientation discrimination in the mouse. *Sci Rep* 5:15830.
16. Hansel D, van Vreeswijk C (2012) The mechanism of orientation selectivity in primary visual cortex without a functional map. *J Neurosci* 32(12):4049–4064.
17. Runyan CA, et al. (2010) Response Features of Parvalbumin-Expressing Interneurons Suggest Precise Roles for Subtypes of Inhibition in Visual Cortex. *Neuron* 67(5):847–857.
18. Liu Bh, et al. (2009) Visual Receptive Field Structure of Cortical Inhibitory Neurons Revealed by Two-Photon Imaging Guided Recording. *J Neurosci* 29(34):10520–10532.
19. Pattadkal JJ, Mato G, van Vreeswijk C, Priebe NJ, Hansel D (2018) Emergent orientation selectivity from random networks in mouse visual cortex. *Cell Rep.* 24(8):2042 – 2050.e6.